



**HAL**  
open science

## Compaction and Permeability Evolution of Tuffs From Krafla Volcano (Iceland)

Michael Heap, Kamal Bayramov, Gabriel Meyer, Marie Violay, Thierry Reuschlé, Patrick Baud, H. Albert Gilg, Claire Harnett, Alexandra Kushnir, Francesco Lazari, et al.

► **To cite this version:**

Michael Heap, Kamal Bayramov, Gabriel Meyer, Marie Violay, Thierry Reuschlé, et al.. Compaction and Permeability Evolution of Tuffs From Krafla Volcano (Iceland). *Journal of Geophysical Research : Solid Earth*, 2024, 129 (8), pp.e2024JB029067. 10.1029/2024JB029067 . hal-04670787

**HAL Id: hal-04670787**

**<https://hal.science/hal-04670787v1>**

Submitted on 13 Aug 2024

**HAL** is a multi-disciplinary open access archive for the deposit and dissemination of scientific research documents, whether they are published or not. The documents may come from teaching and research institutions in France or abroad, or from public or private research centers.

L'archive ouverte pluridisciplinaire **HAL**, est destinée au dépôt et à la diffusion de documents scientifiques de niveau recherche, publiés ou non, émanant des établissements d'enseignement et de recherche français ou étrangers, des laboratoires publics ou privés.

# JGR Solid Earth

## RESEARCH ARTICLE








10.1029/2024JB029067

## Compaction and Permeability Evolution of Tuffs From Krafla Volcano (Iceland)



### Key Points:

- Tuffs are likely weakened by the presence clay minerals, chlorite, and zeolites due to a reduction in fracture toughness
- Permeability of tuff decreases during hydrostatic pressurization, particularly following the onset of inelastic hydrostatic compaction
- Permeability of tuff can increase during ductile deformation due to flow-parallel microcracks that form surrounding collapsed pores

Michael J. Heap<sup>1,2,3</sup> , Kamal Bayramov<sup>1,4</sup>, Gabriel G. Meyer<sup>3</sup> , Marie E. S. Violay<sup>3</sup> , Thierry Reuschlé<sup>1</sup>, Patrick Baud<sup>1</sup> , H. Albert Gilg<sup>5</sup> , Claire E. Harnett<sup>6</sup>, Alexandra R. L. Kushnir<sup>7</sup> , Francesco Lazari<sup>3</sup> , and Anette K. Mortensen<sup>8</sup>

<sup>1</sup>Université de Strasbourg, CNRS, Institut Terre et Environnement de Strasbourg, UMR 7063, Strasbourg, France, <sup>2</sup>Institut Universitaire de France (IUF), Paris, France, <sup>3</sup>Laboratory of Experimental Rock Mechanics, Ecole Polytechnique Fédérale de Lausanne, Lausanne, Switzerland, <sup>4</sup>UNISTRA, Azerbaijan State Oil and Industry University, French Azerbaijani University, Baku, Azerbaijan, <sup>5</sup>Department of Civil, Geo and Environmental Engineering, Technical University of Munich, Munich, Germany, <sup>6</sup>UCD School of Earth Sciences, University College Dublin, Dublin, Ireland, <sup>7</sup>Rock Physics and Geofluids Laboratory, École Polytechnique Fédérale de Lausanne, Lausanne, Switzerland, <sup>8</sup>Landsvirkjun, National Power Company of Iceland, Reykjavik, Iceland

### Supporting Information:

Supporting Information may be found in the online version of this article.

### Correspondence to:

M. J. Heap,  
heap@unistra.fr

### Citation:

Heap, M. J., Bayramov, K., Meyer, G. G., Violay, M. E. S., Reuschlé, T., Baud, P., et al. (2024). Compaction and permeability evolution of tuffs from Krafla volcano (Iceland). *Journal of Geophysical Research: Solid Earth*, 129, e2024JB029067. <https://doi.org/10.1029/2024JB029067>

Received 7 MAR 2024

Accepted 5 AUG 2024

### Author Contributions:

**Conceptualization:** Michael J. Heap

**Formal analysis:** Michael J. Heap, Kamal Bayramov, Thierry Reuschlé, Patrick Baud, H. Albert Gilg

**Funding acquisition:** Michael J. Heap, Marie E. S. Violay

**Investigation:** Michael J. Heap, Kamal Bayramov, Gabriel G. Meyer, Thierry Reuschlé, H. Albert Gilg, Francesco Lazari

**Methodology:** Michael J. Heap

**Project administration:** Michael J. Heap, Marie E. S. Violay

**Resources:** Michael J. Heap, Marie E. S. Violay, Anette K. Mortensen

**Abstract** Pressure and stress perturbations associated with volcanic activity and geothermal production can modify the porosity and permeability of volcanic rock, influencing hydrothermal convection, the distribution of pore fluids and pressures, and the ease of magma outgassing. However, porosity and permeability data for volcanic rock as a function of pressure and stress are rare. We focus here on three porous tuffs from Krafla volcano (Iceland). Triaxial deformation experiments showed that, despite their very similar porosities, the mechanical behavior of the three tuffs differs. Tuffs with a greater abundance of phyllosilicates and zeolites require lower stresses for inelastic behavior. Under hydrostatic conditions, porosity and permeability decrease as a function of increasing effective pressure, with larger decreases measured at pressures above that required for cataclastic pore collapse. During differential loading in the ductile regime, permeability evolution depends on initial microstructure, particularly the initial void space tortuosity. Cataclastic pore collapse can disrupt the low-tortuosity porosity structure of high-permeability tuffs, reducing permeability, but does not particularly influence the already tortuous porosity structure of low-permeability tuffs, for which permeability can even increase. Increases in permeability during compaction, not observed for other porous rocks, are interpreted as a result of a decrease in void space tortuosity as microcracks surrounding collapsed pores connect adjacent pores. Our data underscore the importance of initial microstructure on permeability evolution in volcanic rock. Our data can be used to better understand and model fluid flow at geothermal reservoirs and volcanoes, important to optimize geothermal exploitation and understand and mitigate volcanic hazards.

**Plain Language Summary** The volcanic rocks within a volcano or geothermal reservoir are frequently subject to changes in pressure and stress. Understanding whether pressures and stresses increase or decrease permeability, and by how much, is important for understanding volcano behavior and to maximize the efficiency of a geothermal reservoir. We performed experiments in which we measured the permeability evolution of porous volcanic rocks, three tuffs, as a function of pressure and stress. We also characterized their mechanical behavior. We first show that their mechanical behavior depends on composition: the more clay minerals and chlorite present, the weaker the tuff. We then show that increasing hydrostatic pressure (i.e., depth) decreases their permeability, but that differential loading in the ductile regime can either decrease or increase permeability. Rock permeability usually decreases during deformation in the ductile regime, and so the latter result is surprising. The observed differences in permeability evolution during ductile deformation is attributed to microstructural differences between the tuffs. However, changes in permeability as a function of pressure and stress are small when compared to other rocks, suggesting that tuff may help to maintain hydrothermal circulation in volcanoes and geothermal reservoirs, with attendant consequences for volcanic hazards and geothermal energy exploitation.

© 2024. The Author(s).

This is an open access article under the terms of the [Creative Commons Attribution License](https://creativecommons.org/licenses/by/4.0/), which permits use, distribution and reproduction in any medium, provided the original work is properly cited.

[Attribution License](https://creativecommons.org/licenses/by/4.0/), which permits use, distribution and reproduction in any medium, provided the original work is properly cited.

## 1. Introduction

The permeability—the ease with which fluid can travel through a porous medium—of volcanic rock exerts control over the efficiency of fluid flow within a volcanic structure (e.g., edifice or caldera) or reservoir and, therefore, influences large-scale hydrothermal circulation and convection (Carlino et al., 2018; Ingebritsen

**Supervision:** Michael J. Heap, Marie E. S. Violay  
**Validation:** Michael J. Heap  
**Visualization:** Michael J. Heap  
**Writing – original draft:** Michael J. Heap  
**Writing – review & editing:** Michael J. Heap, Kamal Bayramov, Gabriel G. Meyer, Marie E. S. Violay, Thierry Reuschlé, Patrick Baud, H. Albert Gilg, Claire E. Harnett, Alexandra R. L. Kushnir, Francesco Lazari, Anette K. Mortensen

et al., 2010; Manning & Ingebritsen, 1999; Sammel et al., 1988; Todesco et al., 2003) and the distribution of pore fluids and pore fluid pressures (Ball et al., 2018; Day, 1996; Hurwitz et al., 2003; Reid, 2004). In volcanic structures, the presence of water is known to reduce the strength of volcanic rocks due to chemical effects (Heap & Violay, 2021; Zhu et al., 2016) and, mechanically, high pore fluid pressures in edifice rock can promote flank instability and collapse (Day, 1996; Heap et al., 2021a; Reid, 2004). The ease with which magmatic volatiles can outgas into the adjacent host rock also depends on the permeability of the system (Chevalier et al., 2017; Collinson & Neuberg, 2012), and impeding outgassing can generate high pore pressures and render the system prone to magmatic fragmentation and erratic explosive behavior (Heap et al., 2019; Koyaguchi et al., 2008; Martel et al., 2001; Spieler et al., 2004; Zhang, 1999). In volcanic geothermal reservoirs, the productivity of the geothermal resource is governed by the efficiency of large-scale hydrothermal convection (Huenges and Ledru, 2011), and so rock permeability is a metric of interest for hydrothermal convection models designed to optimize production at existing geothermal sites or to prospect new locations for geothermal exploitation (Bauer et al., 2019; Duwiquet et al., 2019; Guillou-Frottier et al., 2013; Hicks et al., 1996; Vallier et al., 2019).

Permeability is influenced by the physical properties of the rock matrix (e.g., porosity) and the structure of the rock-mass (e.g., macroscopic discontinuities). The permeability of rock typically increases as a function of porosity (Bourbie & Zinszner, 1985; Ehrenberg & Nadeau, 2005; Nelson, 1994; Wadsworth et al., 2016), and macroscopic discontinuities serve to increase the permeability of a rock-mass (Heap & Kennedy, 2016; Kushnir et al., 2018; Nara et al., 2011). Permeability can also be influenced by the effective pressure (assumed in this study to equal the confining pressure (i.e., lithostatic pressure) minus the pore fluid pressure, sometimes referred to as “Terzaghi’s principal”), and by elastic and inelastic deformation. For example, decreasing or increasing the effective pressure will increase or decrease, respectively, the permeability of rock (Brace et al., 1968; Darot & Reuschlé, 2000; David et al., 1994; Meng et al., 2019) and a rock-mass (Baghbanan & Jing, 2008; Gangi, 1978; Min et al., 2004). The influence of deformation on permeability depends on whether the rock is deforming in the brittle or ductile regime, and also on the initial properties (e.g., porosity) of the rock. For example, the permeability of low-porosity crystalline rocks increases in the brittle regime (Acosta & Violay, 2020; Mitchell & Faulkner, 2012; Zoback & Byerlee, 1975) and decreases in the ductile regime (Violay et al., 2017), whereas the permeability of high-porosity (>0.10–0.15) rock can decrease during brittle and ductile deformation (Heap et al., 2022; Zhu & Wong, 1997).

The rocks comprising a volcanic structure or geothermal reservoir are often subject to pressure and stress perturbations associated with volcanic activity and geothermal production. For example, the effective pressure acting on volcanic rock can be increased by lava effusion on the surface, or decreased by increases in pore fluid pressure resulting from magma migration (Elsworth & Voight, 1996) and/or hydrothermal alteration (Heap et al., 2021a). The pressurization and/or movement of magma and hydrothermal fluids within a volcanic structure or reservoir can also increase the stresses acting on the volcanic rock (Gudmundsson, 2020; Todesco et al., 2004). And, finally, stresses within a geothermal reservoir can be increased by production and injection, and pore pressures can be increased and decreased by injection (Terakawa, 2014) and production (Segall & Fitzgerald, 1998), respectively. These pressure and stress perturbations can modify the porosity and permeability of rock, with implications for the myriad processes influenced by changes to fluid flow and convection.

However, experiments designed to explore porosity and permeability evolution in volcanic rock as a function of pressure and stress—reviewed in the next section—are rare. In addition, the microstructural variability of volcanic rocks also demands experimental studies on the range of rock types typically encountered in volcanic edifices and geothermal reservoirs and, so far, most studies have focused on lavas.

## 2. The Permeability of Volcanic Rock

The number of experimental studies aimed at understanding the permeability of volcanic rocks has increased in the last decades, exposing not only a very wide range in permeability (from  $<10^{-20}$  to  $>10^{-12}$  m<sup>2</sup>), but also how the varied microstructures of volcanic rocks can influence their permeability (Blower, 2001; Cant et al., 2018; Colombier et al., 2017; Eichelberger et al., 1986; Farquharson et al., 2015; Heap et al., 2017; Klug & Cashman, 1996; Kushnir et al., 2016; Mordensky et al., 2018; Mueller et al., 2005; Rust & Cashman, 2004; Saar & Manga, 1999; Siratovich et al., 2014; Sruoga et al., 2004; Wright et al., 2009). For example, volcanic rocks can either be granular (e.g., tuffs, lithified mixtures of ash and lapilli that form during an explosive eruption) or non-granular (e.g., lavas, rock that forms when molten or partially-molten lava cools following an effusive eruption),

which dictates their original porosity structure and therefore permeability (e.g., Mueller et al., 2005). And, even within the same microstructural family (granular or non-granular), large variations in void space connectivity and tortuosity (e.g., Colombier et al., 2017; Wright et al., 2009), pore size, shape, and preferred orientation (e.g., Blower, 2001; Vairé et al., 2024; Vasseur & Wadsworth, 2017), and microcrack density (e.g., Kushnir et al., 2016) further complicate porosity-permeability relationships.

Fewer experimental studies have sought to understand the influence of effective pressure on the permeability of volcanic rocks (Eggertsson et al., 2020a, 2020b; Fortin et al., 2011; Heap et al., 2014, 2018a, 2022; Loaiza et al., 2012; Nara et al., 2011; Vinciguerra et al., 2005, 2009). For example, Fortin et al. (2011) measured a decrease in permeability of approximately two orders of magnitude (from  $\sim 10^{-16}$  to  $\sim 10^{-18}$  m<sup>2</sup>) in a low-porosity (porosity of 0.047) basalt from Mt Etna (Italy) as effective pressure was increased to 150 MPa. For the same increase in effective pressure, Heap et al. (2022) measured a decrease of only an order of magnitude (from  $\sim 10^{-15}$  to  $\sim 10^{-16}$  m<sup>2</sup>) for a porous (porosity of 0.21) trachyandesite from Volvic (France). The large decrease in permeability observed in the basalt from Mt Etna, compared to the trachyandesite from Volvic, was thought to be due to the high density of pre-existing microcracks in the basalt; these microstructural features are important for permeability but close easily as effective pressure is increased (Heap et al., 2022). Vinciguerra et al. (2009) found that the permeability of two tuffs from Alban Hills (Italy) decreased by a factor of 1–2 as effective pressure was increased to 70 MPa. Experiments have shown that inelastic hydrostatic compaction decreases the permeability of porous tuffs from Campi Flegrei (Italy; Heap et al., 2014) and porous hyaloclastite from Krafla volcano (Iceland; Eggertsson et al., 2020b), but increases the permeability of a porous lava from the Azores (a volcanic archipelago in the mid-Atlantic; Loaiza et al., 2012).

Only a few laboratory investigations have studied the influence of triaxial deformation on the permeability of volcanic rock (Alam et al., 2014; Farquharson et al., 2016, 2017; Fortin et al., 2011; Heap et al., 2015a, 2020a, 2022; Wang et al., 2016). In the brittle regime, Fortin et al. (2011) showed that the permeability of a basalt from Mt Etna increased by approximately a factor of two following the formation of a macroscopic shear fracture. Farquharson et al. (2016) measured a progressive increase in the permeability of three lavas (one basalt and two andesites) as a function of increasing axial strain in the brittle regime. These authors found that permeability increased by up to three orders of magnitude at the maximum imposed inelastic strain of  $\sim 0.11$  (Farquharson et al., 2016). Heap et al. (2022) found that the permeability of trachyandesite from Volvic decreased by a factor of 2–6 up to the peak stress and remained more-or-less constant following macroscopic fracture formation. The permeability of high-porosity tuff (porosity of 0.37) from Shikotsu (Hokkaido, Japan) was found to remain more-or-less constant up to an inelastic strain of  $\sim 0.10$  in the brittle regime (Alam et al., 2014). However, the permeability of tuff with a lower porosity (porosity  $< 0.1$ ) from Newberry volcano (Oregon, USA) increased by several orders of magnitude following deformation in the brittle regime (Wang et al., 2016).

The permeability of porous lava and tuff has been shown to decrease during ductile deformation (Alam et al., 2014; Farquharson et al., 2017; Heap et al., 2015a, 2020a, 2022). The permeability of andesites from Volcán de Colima (Mexico), for example, decreased during ductile deformation by up to two orders of magnitude, depending on the effective pressure and the amount of inelastic strain (Farquharson et al., 2017; Heap et al., 2015a, 2020a). Heap et al. (2022) found that the permeability of trachyandesite from Volvic decreased by up to an order of magnitude as a function of increasing deformation in the ductile regime (up to an axial strain of  $\sim 0.12$ ). The permeability of porous tuff from Shikotsu decreased by about an order of magnitude following deformation up to an inelastic strain of  $\sim 0.08$ – $0.1$  in the ductile regime (Alam et al., 2014). Permeability reductions in lava during ductile deformation were found to be the result of the formation of compaction bands (i.e., planes of collapsed pores orientated sub-perpendicular to the applied differential stress; Loaiza et al., 2012; Heap et al., 2015a, 2020a, 2022; Farquharson et al., 2017). In tuffs, rocks that do not develop compaction bands (Heap et al., 2015b; Heap & Violay, 2021; Zhu et al., 2011), permeability was reduced by the distributed cataclastic collapse of pores (Alam et al., 2014).

Owing to the paucity of experimental studies that provide data on the influence of effective pressure and differential stress on the permeability of tuff, a rock type commonly encountered at volcanoes, we provide here an experimental study in which we (a) measured the permeability (and P-wave velocity) of tuffs as a function of increasing effective pressure (to pressures above the onset of inelastic compaction) and (b) measured the porosity and permeability of tuffs as a function of increasing axial strain in the ductile regime. We also provide a complete mechanical characterization of the studied tuffs to compare with previously published data for tuff. For our study,

we selected three tuffs from boreholes drilled into Krafla volcano, described in detail in the next section. Although we present data for tuff from Krafla volcano, we consider our new data relevant for the permeability structure and evolution of volcanic structures (edifices and calderas) and geothermal reservoirs containing tuffs worldwide.

### 3. Materials and Methods

Krafla volcano, located in Northeast Iceland, is situated on a 90 km-long, NNE-trending fissure zone (Hjartardóttir et al., 2012; Opheim & Gudmundsson, 1989). The volcanic complex includes a 10 km-diameter caldera, partially filled with hyaloclastites, basaltic lavas, and tuffs (Eggertsson et al., 2020a, 2020b; Escobedo et al., 2021; Lévy et al., 2018; Mortensen et al., 2014; Weaver et al., 2020), that hosts a large hydrothermal system (Árnason, 2020; Arnórsson et al., 2008; Gasperikova et al., 2015; Pope et al., 2016). The hydrothermal system has been exploited by numerous geothermal wells to produce electricity since the mid-1970s (Friðleifsson & Elders, 2005; Friðleifsson et al., 2014; Ármannsson et al., 1987). Volcanically-active areas are particularly inviting locations for geothermal exploitation because high-temperature and superheated reservoirs can yield high power outputs (Elders et al., 2014; Reinsch et al., 2017). Krafla volcano is an active volcano and, in the past 3,000 years, fissure eruptions have occurred every 300–1,000 years; the most recent activity was the Krafla Fires of 1975–1984 (Björnsson, 1985; Björnsson et al., 1977; Sæmundsson, 1991).

For this study, three tuffs from different depths were selected from boreholes KH-05 and KH-06: 394.0–394.5 m (KT1; borehole KH-05), 505.5–506.0 m (KT2; borehole KH-05), and 688.9–690.6 m (KT3; borehole KH-06) (borehole locations shown in Figure 1a; Gautason et al., 2007). These samples were selected based on their different depths (corresponding to different predicted alteration zones, see Escobedo et al., 2021) and their different textures and colors. Although tuff is not the most volumetrically important rock type in the caldera-fill stratigraphy at Krafla, porous tuffs are common and are encountered in borehole KH-06 at depths of ~4–6, ~16–20, ~185–190, ~272–298, ~315–318, and ~620–622 m, and in borehole KH-05 at depths of ~36–44, ~97–100, ~130–150, ~367–370, and ~492–494 m (Gautason et al., 2007). Typically, the layers of tuff are several meters in thickness. Detailed stratigraphic logs of boreholes KH-05 and KH-06 can be found in Gautason et al. (2007).

In hand specimen, KT1 is a heterogeneous green-, gray-, and white-colored tuff with a wide particle size distribution (the fragments within the matrix can be up to 10 mm in size), KT2 is a relatively homogenous and fine-grained light-green-colored tuff, and KT3 is a relatively homogenous and fine-grained white-gray-colored tuff (Figures 1b and 1c). Backscattered scanning electron microscope (SEM) images of the intact tuffs show that KT1 and KT2 are composed of angular and sub-spherical fragments (Figures 1d and 1e), and that KT3 is composed of angular fragments (Figure 1f).

A detailed grain size analysis of the matrix (data available as Supporting Information S1; Data Set S1) was performed for each sample by manually drawing around individual grains on SEM images and then analyzing the resulting image using open-source image analysis software ImageJ. The equivalent grain diameter of each grain,  $d$ , was calculated using  $d = 3/2(d_F)$ , where  $d_F$  is the average Feret diameter. Our analysis shows that KT1 has a wide grain size distribution (standard deviation of ~35  $\mu\text{m}$ ), and that most grains are ~45–75  $\mu\text{m}$  in diameter (mean grain diameter is ~73  $\mu\text{m}$ ) (Figure S1 in Supporting Information S1). The majority of grains in KT2 are ~30–50  $\mu\text{m}$  in diameter (mean grain diameter is ~44  $\mu\text{m}$ ) and very few grains are >100  $\mu\text{m}$  in diameter, giving KT2 a narrow grain size distribution (standard deviation of ~22  $\mu\text{m}$ ) (Figure S2 in Supporting Information S1). Although the majority of grains in KT3 are ~10–20  $\mu\text{m}$  in diameter (mean grain diameter is ~45  $\mu\text{m}$ ), the grain size distribution is large (standard deviation of ~49  $\mu\text{m}$ ), giving KT3 a positively skewed grain size distribution (Figure S3 in Supporting Information S1). The pores within the tuffs, the void space between fragments, range from a few microns up to ~500  $\mu\text{m}$  in KT1, up to ~50–70  $\mu\text{m}$  in KT2, and up to ~200  $\mu\text{m}$  in KT3 (Figures 1d, 1e, and 1f).

Quantitative phase analysis of a hand-powdered aliquot of each of the three tuffs was performed using X-ray powder diffraction (XRPD) data and the Rietveld approach (BGMN/Profex, Doebelin & Kleeberg, 2015) (Table 1). The XRPD data are provided in the Supporting Information (Figures S4, S5, and S6 in Supporting Information S1). To ensure that our mineral composition data are representative of the core from which our experimental samples were prepared, the measured aliquot was taken from a large, and well-mixed, mass of powder (~50–100 g). The clay minerals were identified by XRPD using an oriented specimen in an air-dried, ethylene-glycolated and heated (heated to, and cooled from, 550°C) state. In terms of clay minerals, KT1 and KT2 contain 27.3 and 20.9 wt% of mixed-layer chlorite-smectite, respectively, and KT3 contains 15 wt% of mixed-

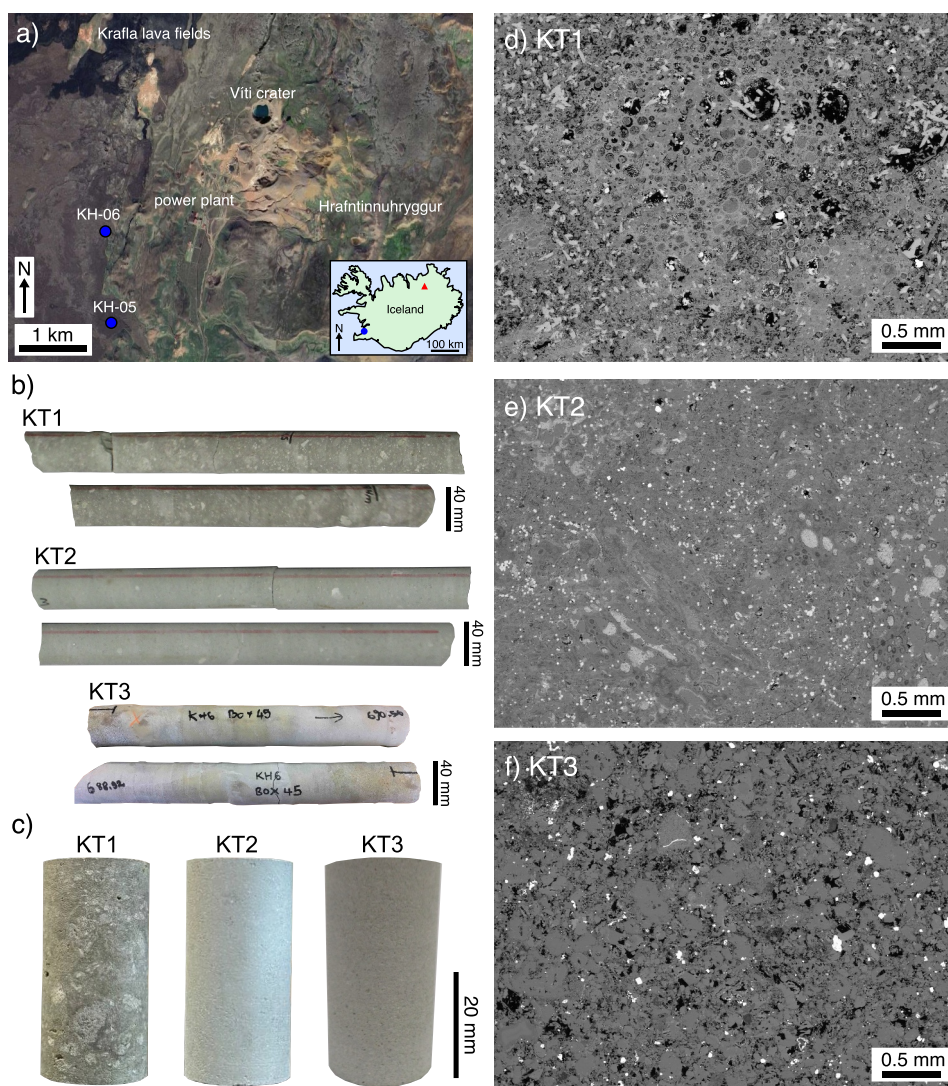


**Figure 1.** (a) GoogleEarth® image showing the location of boreholes KH-05 and KH-06 drilled by Landsvirkjun. The power plant is surrounded by mafic lavas to the north and west, and subglacial hyaloclastites and mafic lavas to the northeast and south. Hrafninnuhryggur, a rhyolitic dyke to the east of the power plant, forms a prominent ridge. See Sæmundsson et al. (2012) for a geologic map of the area. Inset shows a map of Iceland in which the locations of Krafla and Reykjavík are indicated by the red triangle and blue circle, respectively. (b) Photographs of the core material collected from the boreholes. KT1 was collected from KH-05 at a depth of 394.0–394.5 m, KT2 was collected from KH-05 at a depth of 505.5–506.0 m, and KT3 was collected from KH-06 at a depth of 688.9–690.6 m. (c) Photographs of 20 mm-diameter samples of KT1, KT2, and KT3. (d) Backscattered scanning electron microscope (SEM) image of KT1. (e) SEM image of KT2. (f) SEM image of KT3. In the SEM images, black and gray correspond to the porosity and the rock-forming minerals, respectively.

layer R3 ordered illite-smectite (Table 1). Based on a microstructural inspection (Figures 1d, 1e, and 1f), the clay minerals in all three tuffs form part of the matrix between grains (i.e., at the grain contacts), and are also present within some pores (i.e., pore-filling).

Cylindrical samples were cored parallel to the axis of the retrieved core to a diameter of 20 mm. These samples were then cut, precision-ground to a length of ~40 mm (examples are shown in Figure 1c), washed using water, and then vacuum-dried in an oven for 48 hr at a temperature of 40°C. We prepared seven samples of KT1 and 10 samples of KT2 and KT3 (a total of 27 samples). The skeletal volume of each of the 27 samples was measured using a helium pycnometer, which was then used to calculate their connected porosity using their bulk sample volume (measured using digital calipers). Relative uncertainties of measurements of connected porosity are <2%. The solid density of KT1, KT2, and KT3 was calculated by measuring the mass and volume of hand-powdered

**Table 1**  
*Mineral Modes*

Mineral	KT1	KT2	KT3
quartz	29.3	9.2	46.8
albite	11.7	29.7	-
K-feldspar	6.5	6.3	10.4
plagioclase	-	-	13.9
mixed-layer chlorite-smectite	27.3	20.9	-
mixed-layer R3 ordered illite-smectite	-	-	15.0
epidote	17.1	2.6	-
actinolite	-	19.6	-
titanite	8.0	8.6	-
wairakite	-	-	6.7
pyrite	0.3	-	4.0
chlorite	-	-	2.8
calcite	-	3.4	-
gypsum	-	-	0.4

*Note.* Mineral modes, measured by X-ray powder diffraction (XRPD), for the three tuffs collected from Krafla for this study. Values in wt%. <sup>a</sup>Trace gypsum in KT3 likely formed following the oxidation of pyrite following core retrieval.

offcuts using, respectively, an electronic balance and the helium pycnometer. The total porosity of each of the 27 samples was then determined using the dry bulk density of each sample and the solid density of the parent core. The isolated porosity of each sample was then calculated by subtracting the connected porosity from the total porosity. All of the 20 mm-diameter samples were then vacuum-saturated with de-aired, deionized water. We performed three sets of laboratory experiments for this study: (a) hydrostatic experiments in which we measured P-wave velocity and permeability as a function of effective pressure (performed at the Strasbourg Institute of Earth and Environment (ITES, France)), (b) uniaxial and triaxial deformation experiments (performed at the ITES), and (c) triaxial deformation experiments in which we measured permeability during deformation (performed at the Laboratory of Experimental Rock Mechanics (LEMUR) at the École Polytechnique Fédérale de Lausanne (Switzerland)).

The P-wave velocities and permeabilities of one water-saturated 20 mm-diameter sample of each of the three tuffs (Table 2) were measured under ambient laboratory temperature as a function of increasing effective pressure at ITES. A schematic diagram of the device is provided in Figure S7a in Supporting Information S1. Each sample was inserted into a Viton® jacket and then placed inside the hydrostatic pressure vessel. The confining pressure (oil) was then increased to 1 MPa. Following microstructural equilibration at the target effective pressure, P-wave velocity was measured using the sample length and the corrected (i.e., corrected for the transit time through the metal endcaps) transit time between two piezoceramic transducers housed within

steel endcaps in contact with the top and bottom of the sample. The transmitting transducer was excited (a sinusoidal pulse with a frequency of 700 kHz) by an Agilent 33220A 20 MHz Function/Arbitrary Waveform Generator, and the signal from the receiving transducer was amplified using a preamplifier from Physical Acoustics. The amplified signal from the receiving transducer was digitally stored using an oscilloscope (sampling rate 500 MHz; data available as Supporting Information; Data Sets S2, S3, and S4) and the transit time was manually picked as the first deviation from the background signal. The permeability of the sample was then measured using either the steady-state (for high permeability measurements) or pulse-decay (for low permeability measurements) method. For the steady-state method, we imposed a pore pressure differential ( $P_u - P_d$ ) of 0.5 MPa along the length of the sample (i.e., in the same direction as the measurements of P-wave velocity) and the mass of water flowing out of the sample was measured over time (using an electronic balance with a precision of  $\pm 0.0005$  g), which was converted to a volumetric flow rate,  $Q$ , using the density of water at ambient conditions (data available as Supporting Information; Data Sets S2, S3, and S4). Permeability,  $k$ , was determined using Darcy's law once the volumetric flow rate was constant (i.e., steady-state flow):

$$\frac{Q}{A} = \frac{k}{\mu L}(P_u - P_d) \quad (1)$$

where  $\mu$  is the viscosity of the pore fluid, and  $A$  and  $L$  are the cross-sectional area and length of the sample, respectively (all assumed to be constant). For the pulse-decay measurements, we monitored the pressure decay of an upstream reservoir (at a starting pore pressure differential of 0.5 MPa) of known volume (data available as Supporting Information; Data Sets S2, S3, and S4). Permeability was then determined using (Brace et al., 1968):

$$\Delta P_p(t) \propto \exp(-\alpha t) \quad (2)$$

$$\alpha = \frac{Ak(C_u + C_d)}{\mu LC_u C_d} \quad (3)$$

where  $\Delta P_p$  is the change in pore fluid pressure,  $t$  is time, and  $C_u$  and  $C_d$  are the compressive storages of the upstream and downstream pore pressure circuits, respectively, defined as the ratios of the change in fluid volume corresponding to the pore pressure variation ( $C = \partial V / \partial P_p$ ). When the downstream pore pressure is connected to

**Table 2**  
*Experimental Summary*

Sample	Test type	Connected porosity	Total porosity	Confining pressure (MPa)	Pore fluid pressure (MPa)	Effective pressure (MPa)	Peak differential stress (MPa)	$C^*$ (MPa)	$P^*$ (MPa)
KT1_6	Hydrostatic	0.33	0.33	hydro	10	hydro	-	-	23
KT1_5	Uniaxial	0.34	0.34	0	0 (wet)	0	14.8	-	-
KT1_2	Uniaxial	0.34	0.34	0	0 (dry)	0	40.2	-	-
KT1_4	Triaxial	0.33	0.33	15	10	5	19.5	-	-
KT1_3	Triaxial	0.35	0.35	20	10	10	24.3	-	-
KT1_7	Triaxial	0.35	0.35	25	10	15	-	14.5	-
KT1_1	Hydrostatic + P-wave + permeability	0.34	0.34	≤60	-	≤60	-	-	20–25
KT1_1 EPFL	Triaxial + permeability	0.35	0.35	25	10	15	-	12.8	-
KT2_7	Hydrostatic	0.33	0.33	hydro	10	hydro	-	-	46
KT2_5	Uniaxial	0.33	0.33	0	0 (wet)	0	32.8	-	-
KT2_2	Uniaxial	0.34	0.34	0	0 (dry)	0	64.7	-	-
KT2_3	Triaxial	0.35	0.35	15	10	5	36.7	-	-
KT2_4	Triaxial	0.33	0.33	20	10	10	47.9	-	-
KT2_8	Triaxial	0.34	0.34	25	10	15	46.0	-	-
KT2_6	Triaxial	0.34	0.34	30	10	20	-	34.9	-
KT2_9	Triaxial	0.33	0.33	35	10	25	-	29.7	-
KT2_10	Triaxial	0.33	0.33	45	10	35	-	21.3	-
KT2_1	Hydrostatic + P-wave + permeability	0.33	0.33	≤60	-	≤60	-	-	45–50
KT2_1 EPFL	Triaxial + permeability	0.33	0.33	40	10	30	-	24.7	-
KT3_9	Hydrostatic	0.30	0.29	hydro	10	hydro	-	-	38
KT3_7	Uniaxial	0.29	0.29	0	0 (wet)	0	19.2	-	-
KT3_10	Uniaxial	0.31	0.30	0	0 (dry)	0	32.3	-	-
KT3_1	Triaxial	0.29	0.29	15	10	5	31.8	-	-
KT3_4	Triaxial	0.30	0.30	20	10	10	29.7	-	-
KT3_3	Triaxial	0.28	0.29	25	10	15	-	28.9	-
KT3_5	Triaxial	0.28	0.28	30	10	20	-	24.8	-
KT3_6	Triaxial	0.28	0.28	35	10	25	-	20.6	-
KT3_2	Triaxial	0.28	0.28	40	10	30	-	14.1	-
KT3_8	Hydrostatic + P-wave + permeability	0.29	0.29	≤60	-	≤60	-	-	35–45
KT3_1 EPFL	Triaxial + permeability	0.28	0.28	35	10	25	-	17.2	-
KT3_3 EPFL	Triaxial + permeability	0.30	0.30	35	10	25	-	20.1	-

*Note.* Summary of the deformation experiments performed for this study.  $C^*$  - differential stress required for the onset of shear-enhanced compaction;  $P^*$  - differential pressure required for the onset of hydrostatic inelastic compaction<sup>a</sup>. <sup>a</sup>Samples simply labeled with a number (e.g., KT1\_1) are 20 mm-diameter samples measured in Strasbourg (France) and samples labeled with “EPFL” (e.g., KT1\_1\_EPFL) are 37 mm-diameter samples measured at EPFL (Lausanne, Switzerland).

the atmosphere, as in our setup,  $1/C_d = 0$ , and  $\alpha = Ak/\mu LC_u$ . P-wave velocity and permeability measurements were made during pressurization to and from a confining pressure of 60 MPa.

Triaxial deformation experiments (i.e.,  $\sigma_1 > \sigma_2 = \sigma_3$ ; where  $\sigma_1$ ,  $\sigma_2$ ,  $\sigma_3$  are the maximum, intermediate, and minimum principal stresses, respectively) were performed on 20 mm-diameter samples of each of the three tuffs at a range of effective pressures,  $P_e$ , from 5 to 35 MPa (using a pore fluid pressure,  $P_p$ , of 10 MPa), at ITES (Table 2) (a schematic diagram of the device is provided in Figure S7b in Supporting Information S1).  $P_e$  is assumed here to be  $P_e = P_c - P_p$ , where  $P_c$  is the confining pressure. All experiments were performed at ambient laboratory temperature. The confining (oil) and pore fluid (deionized water) pressures were slowly increased to



the target pressures using servo-controlled pumps equipped with encoders (manufactured by Nova Swiss). After the target pressure was reached, the sample was left to equilibrate at the target effective pressure (i.e., until the porosity of the sample had reached a constant value). The samples were then deformed at an axial strain rate of  $10^{-5} \text{ s}^{-1}$ . Experiments were stopped following macroscopic failure in the case of the brittle experiments (indicated by a stress drop) or, if the behavior was assumed to be ductile (i.e., there was no stress drop), at an axial strain of 4%. We define brittle experiments as those that failed by the formation of a macroscopic shear fracture. Ductile behavior is defined here as the capacity of a rock to deform to large strains without macroscopic shear fracture formation. We consider that these failure modes describe the mechanical behavior on the sample lengthscale, and that they are independent of deformation micromechanism (see Wong and Baud (2012) and Heap and Violay (2021) for further discussion on failure mode). During the experiments, axial load was measured using the oil pressure inside a pressurized chamber above the pressure vessel, the chamber diameter, and the diameter of the piston. Axial displacement was measured using an external linear variable differential transducer (LVDT). Axial load and displacement were then converted to axial stress and strain using the original sample radius and length. Pore volume change (i.e., the change in sample porosity) was also calculated using data from the pore pressure encoder. Signals from all transducers were digitized using a Keithley 2000 Series Multimeter and stored and displayed using a LabVIEW program.

We performed additional experiments in the triaxial deformation apparatus at ITES (Figure S7b in Supporting Information S1). First, we performed uniaxial (i.e.,  $P_c$  and  $P_p$  were equal to zero) experiments on oven-dried and water-saturated samples of each tuff (Table 2). Second, we performed a hydrostatic experiment (i.e.,  $\sigma_1 = \sigma_2 = \sigma_3$ ) on a sample of each tuff in which we measured sample porosity change during hydrostatic pressurization (using a  $P_p$  of 10 MPa) (Table 2). Confining pressure was increased in small steps (2–10 MPa) during the hydrostatic experiment, and the next pressure increment was only applied following the microstructural equilibrium of the sample. All data for the uniaxial and triaxial experiments performed at ITES are available as Supporting Information (Data Sets S5, S6, and S7).

A final set of experiments was performed on 37 mm-diameter samples (precision-ground to a length of ~77–83 mm) of each tuff using FIRST (Fluid Induced eaRthquake SimulaTor), a triaxial deformation apparatus at the LEMR (Cornelio & Violay, 2020; Heap et al., 2022; Noël et al., 2021a; a schematic diagram of the device is provided in Figure S7c in Supporting Information S1) (Table 2). During these experiments, permeability was measured parallel to the axis of the cylindrical sample during constant strain rate deformation under an effective pressure corresponding to the ductile regime, guided by the experiments performed at ITES. Each sample was first saturated with de-aired and deionized water, sandwiched between two pore fluid distribution plates (3 mm-thick), inserted in a Viton® jacket, and then placed inside the pressure vessel. Independently controlled servo-controlled pore fluid pressure pumps, equipped with encoders, were connected to the top (upstream) and bottom (downstream) of the sample. The vessel was closed and the confining pressure (oil) and pore fluid (deionized water) pressure were increased to 12 and 10 MPa, respectively. Following microstructural equilibration, permeability was measured at  $P_e = 2$  MPa. First, the downstream and upstream pore fluid pressure pumps were set to constant pore fluid pressures of 9.5 and 10.5 MPa, respectively (pore pressure differential of 1 MPa). The volumetric flow rate of water moving through the sample was tracked by the pore fluid pressure pump encoders. Permeability was calculated using Darcy's law (Equation 1) once steady-state flow was established. The pore fluid pressure pumps were then set to 10 MPa and one was isolated from the sample. By isolating one of the pore fluid pressure pumps, porosity change during hydrostatic pressurization can be accurately calculated using the encoder of the connected pump. Sample permeability was measured, as described above, at several pressures up to the target effective pressure for the deformation experiments.

After microstructural equilibration at the target effective pressure, the samples were deformed at a constant strain rate of  $10^{-5} \text{ s}^{-1}$ . During deformation, only one pore fluid pressure pump (set to a constant pressure of 10 MPa) was connected to the sample so as to measure porosity change. Axial strain was calculated using the initial sample length and the average displacement measured by two internal LVDTs. A hemispherical seat, positioned on top of the upper endcap, ensured that there was no misalignment during loading. Axial stress was calculated using the pressure acting on the piston, the area of the top of the piston, and the original sample radius. Sample permeability was measured intermittently during deformation. To measure permeability, the position of the piston was halted, both pore fluid pressure pumps were connected to the sample, a pore pressure differential of 1 MPa was set between the pumps, and permeability was determined as described above. Once permeability was measured, the

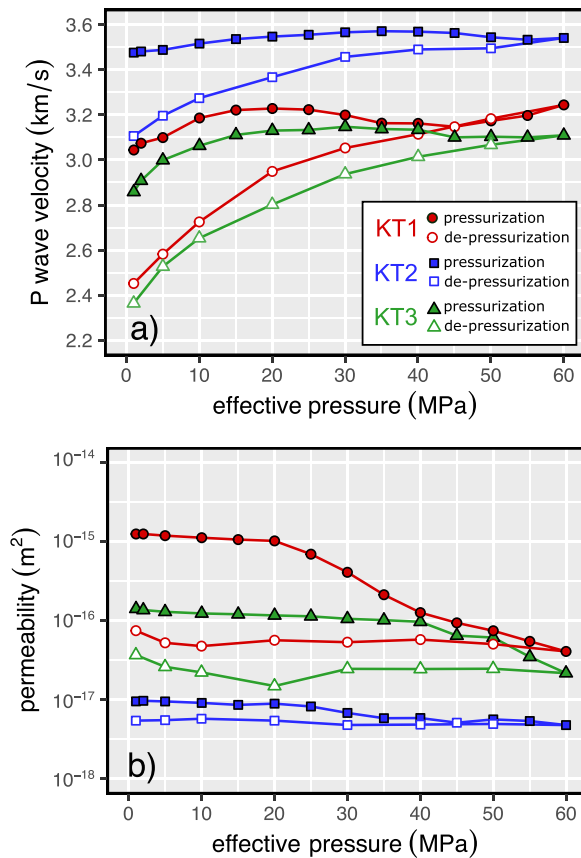


**Figure 2.** P-wave velocity (a) and permeability (b) as a function of effective pressure during the hydrostatic pressurization (filled symbols) and depressurization (unfilled symbols) of samples of water-saturated tuff from Krafla volcano (KT1, KT2, and KT3). The relative error on our permeability measurements is <1% (i.e., within the symbol size).

pore pressures were set back to 10 MPa, one pump was isolated from the sample, and deformation was restarted. This method was continued up to an axial strain of 0.11–0.13. The method described here has been used previously used to measure the permeability of porous lava (Heap et al., 2022), porous limestones (Meng et al., 2019), and porous sandstones (Baud et al., 2012; Fortin et al., 2005; Zhu & Wong, 1997) during deformation. All data for the triaxial experiments performed at EPFL are available as Supporting Information (Data Sets S8, S9, S10, and S11).

## 4. Results

### 4.1. Porosity

The connected porosity of the samples of tuff was measured to be 0.33–0.35, 0.33–0.34, and 0.28–0.31 for KT1, KT2, and KT3, respectively (Table 2). The solid densities of KT1, KT2, and KT3 were measured to be 2,959.4, 2,907.6, and 2,691.9 kg/m<sup>3</sup>, respectively, yielding total porosities that are essentially the same as the measured connected porosities (Table 2). In other words, there is little to no isolated porosity in the studied tuffs.

### 4.2. P-Wave Velocity and Permeability Under Hydrostatic Conditions

The evolution of P-wave velocity and permeability as a function of effective pressure for samples of KT1, KT2, and KT3 is shown in Figures 2a and 2b, respectively. During pressurization, the P-wave velocity of each tuff first increased (Figure 2a). Then, at a threshold effective pressure—25 MPa for KT1, 45 MPa for KT2, and 40 MPa for KT3—P-wave velocity decreased. The P-wave velocity of KT2 and KT3 decreased up to the maximum effective pressure of 60 MPa (Figure 2a). However, the P-wave velocity of KT1 increased as the effective pressure was increased from 45 to 60 MPa (Figure 2a). During depressurization, the P-wave velocity of each tuff decreased (Figure 2a). We also note that the P-wave velocity for a given pressure during depressurization was much lower than during pressurization (Figure 2a). For example, at 1 MPa, the P-wave velocity of KT1, KT2, and KT3 during depressurization was 0.59, 0.37, and 0.49 km/s slower than during pressurization, respectively (Figure 2a).

The permeability of KT1 and KT3 decreased modestly up to a threshold effective pressure of 20 and 40 MPa, respectively (Figure 2b). Above these threshold pressures, there was a pronounced increase in the reduction of permeability of KT1 and KT3 per unit pressure as a function of effective pressure (Figure 2b). This is especially true for KT1, the permeability of which decreased from  $1.03 \times 10^{-15}$  to  $4.09 \times 10^{-17}$  m<sup>2</sup> as effective pressure was increased from 20 to 60 MPa (Figure 2b). The permeability of KT2, however, decreased steadily as the effective pressure was increased from 1 to 60 MPa, without a pronounced increase in the reduction of permeability per unit pressure as a function of effective pressure (Figure 2b). The permeability of KT2 only decreased from  $9.53 \times 10^{-18}$  to  $4.77 \times 10^{-18}$  m<sup>2</sup> as effective pressure was increased from 1 to 60 MPa (Figure 2b). During depressurization, the permeability of KT1 and KT3 remained more-or-less constant as effective pressure was reduced to ~20 MPa (Figure 2b). At pressures below ~20 MPa, the permeability of KT1 and KT3 increased as the effective pressure was decreased to 1 MPa (Figure 2b). The permeability of KT2, however, remained more-or-less constant as effective pressure was reduced from 60 to 1 MPa (Figure 2b). We also note that the permeability for a given pressure during depressurization was often much lower than during pressurization (Figure 2b). For example, at 1 MPa, the permeability of KT1, KT2, and KT3 during depressurization was a factor of 16.8, 1.8, and 3.9 lower than during pressurization, respectively (Figure 2b).

### 4.3. Triaxial Deformation Experiments

Stress-strain curves, and porosity reduction as a function of axial strain, for the deformation experiments performed at  $P_e$  between 0 (i.e., uniaxial) and 35 MPa are shown in Figure 3. The experiments performed on

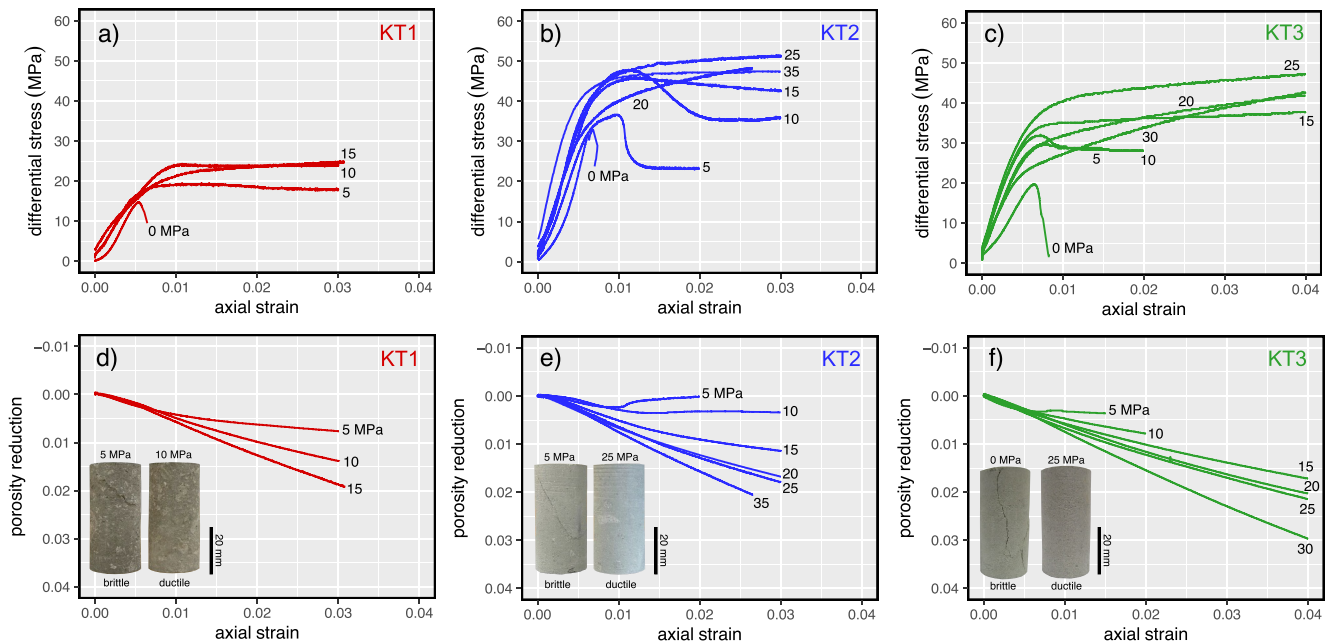


**Figure 3.** (a), (b), and (c) Stress-strain curves for three tuffs from Krafla volcano (KT1, KT2, and KT3) deformed at different effective pressures (provided next to each curve). (d), (e), and (f) Porosity reduction as a function of axial strain for the experiments shown in panels (a), (b), and (c). The effective pressure is provided next to each curve. Insets show photographs of samples deformed in the brittle regime and the ductile regime. Shear fractures are shown for KT1 and KT2 (at effective pressures of 5 MPa) and axial splits are shown for KT3 (at an effective pressure of 0 MPa).

KT1, KT2, and KT3 at  $P_e = 0\text{--}5$  MPa,  $P_e = 0\text{--}15$  MPa, and  $P_e = 0\text{--}10$  MPa, respectively, can be classified as brittle: their stress-strain curves are characterized by peak stresses and strain softening (Figures 3a, 3b, and 3c), and the post-deformation samples contained shear fractures at  $P_e > 0$  MPa or axial splits at  $P_e = 0$  MPa (see insets on Figures 3d, 3e, and 3f). Although the samples deformed under these effective pressures were brittle, the porosity of these samples decreased during deformation (Figures 3d, 3e, and 3f). The experiments performed on KT1, KT2, and KT3 at  $P_e \geq 10$  MPa,  $P_e \geq 20$  MPa, and  $P_e \geq 15$  MPa, respectively, can be classified as ductile: their stress-strain curves are characterized by strain hardening and an absence of a peak stress (Figures 3a, 3b, and 3c), and the post-deformation samples did not contain shear fractures (see insets on Figures 3d, 3e, and 3f). The porosity of the samples deformed in the ductile regime decreased as a function of axial strain and, for a given axial strain, a larger decrease was observed at higher  $P_e$  (Figures 3d, 3e, and 3f). These data highlight that the effective pressure required for ductile behavior is the lowest for KT1 and highest for KT2 (Figure 3).

Effective mean stress,  $P$ , defined as  $P = (\sigma_1 + \sigma_2 + \sigma_3)/3 - P_p$ , is plotted as a function of porosity reduction for the experiments performed on samples of KT1, KT2, and KT3 in Figures 4a, b, and 4c, respectively. Figure 4 includes data for the hydrostatic experiments (black dashed lines) and the triaxial deformation experiments (solid colored lines). The onset of inelastic compaction during the hydrostatic experiments,  $P^*$ , occurred at a pressure of 23, 46, and 38.8 MPa for KT1, KT2, and KT3, respectively (Figure 4; Table 2). The position at which the triaxial curves deviate from that of the hydrostatic indicates the onset of inelastic deformation. Deviations to the left of the curve (i.e., an increase in porosity) indicate the onset of dilatational microcracking, termed  $C'$ , and deviations to the right (i.e., a decrease in porosity) indicate the onset of shear-enhanced compaction, termed  $C^*$  (Figure 4).

A plot of the differential stress at failure as a function of the effective mean stress at failure shows the failure envelope and compactive yield cap for the three tuffs from Krafla (Figure 5). The peak stress maps out the failure envelope in the brittle regime, and  $C^*$  maps out the yield cap in the ductile regime (with  $P^*$  at  $Q = 0$ ) (see review by Wong & Baud, 2012). These diagrams, so-called “ $P$ - $Q$  plots”, are a convenient way to compare the mechanical behavior of rocks. Figure 5 shows that the stresses required for brittle failure, the onset of shear-

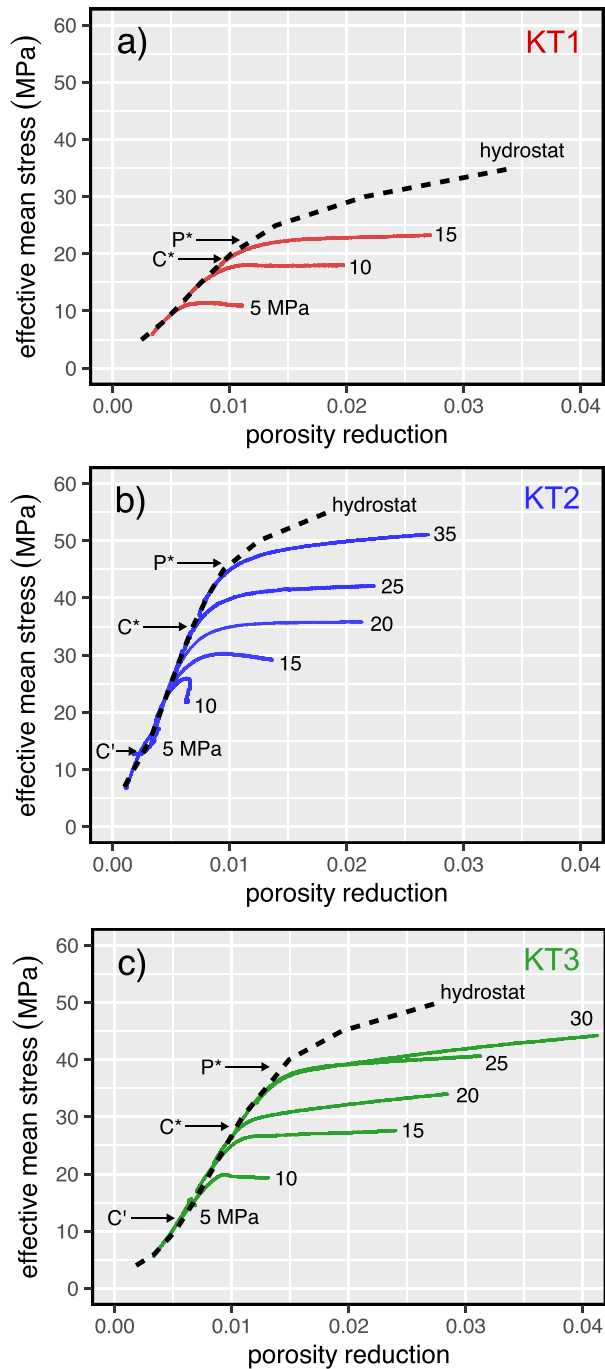


**Figure 4.** Effective mean stress as a function of porosity reduction for the triaxial experiments performed on samples of (a) KT1, (b) KT2, (c) KT3 (colored solid lines), alongside data from hydrostatic experiments performed on each tuff (thick black dashed lines). The effective pressure is provided next to each curve. The onset of inelastic compaction in the hydrostatic experiments,  $P^*$ , and examples of the onset of shear-enhanced compaction,  $C^*$ , and dilatational microcracking,  $C'$ , are labeled on relevant triaxial curves.

enhanced compaction ( $C^*$ ), and the onset of inelastic hydrostatic compaction ( $P^*$ ) are lowest for KT1 and highest for KT2.

#### 4.4. Influence of Deformation in the Ductile Regime on Permeability

We performed four triaxial deformation experiments in which we measured permeability during deformation at an effective pressure corresponding to the ductile regime (15, 30, and 25 MPa for KT1, KT2, and KT3, respectively). Two experiments were performed on samples of KT3 at the same effective pressure to check for reproducibility. The stress-strain curves for the experiments are shown in Figure 6a, which are qualitatively similar to the stress-strain curves shown in Figure 3. The experiments shown in Figure 6a also show that, at higher axial strains, there is a gradual reduction in the rate of strain hardening for KT3, but not for KT1 and KT2. Porosity reduction as a function of axial strain is shown in Figure 6b; these curves are also qualitatively similar to the porosity reduction curves shown in Figure 3. The porosity data of Figure 6b show that the decrease in the rate of strain hardening in KT3 (Figure 6a) was also accompanied by a decrease in the rate of porosity reduction. Finally, permeability as a function of axial strain is shown in Figure 6c. For KT1, permeability decreased continuously, from  $1.45 \times 10^{-15}$  to  $2.49 \times 10^{-16}$  m<sup>2</sup>, up to the maximum axial strain of  $\sim 0.13$  (Figure 6c). For KT2, permeability decreased from  $7.71 \times 10^{-18}$  to  $6.22 \times 10^{-18}$  m<sup>2</sup> as axial strain was increased from 0 to  $\sim 0.009$  (Figure 6c). The permeability of KT2 remained more-or-less constant at axial strains above  $\sim 0.009$ , although we note that permeability increased very slightly from an axial strain of  $\sim 0.1$  to the maximum axial strain of  $\sim 0.135$  (Figure 6c). For KT3, permeability decreased very slightly at low strain, and then increased slightly up to the maximum axial strain (Figure 6c). The increase in permeability during deformation is more pronounced in sample KT3\_1\_EPFL than in sample KT3\_3\_EPFL (Figure 6c). In summary, while the permeability of KT1 decreased during deformation by about a factor of six, the permeability of KT2 and KT3 did not change appreciably during deformation in the ductile regime (Figure 6c). The mechanical behavior and permeability evolution of the two KT3 experiments were found to be very similar (Figure 6), although we note that there is a slight difference in the evolution of porosity during deformation (Figure 6b).

The complete evolution of porosity and permeability during the experiments shown in Figure 6 (i.e., including the hydrostatic pressurization and depressurization) is shown in Figure 7. For all samples, porosity and permeability decreased during hydrostatic pressurization (Figure 7). For KT1, porosity and permeability decreased during differential stress loading, and then increased during depressurization (Figure 7). The permeability of KT1 was lower at the end of the experiment than at the start (Figure 7). For KT2, however, porosity decreased while permeability remained more-or-less constant during differential stress loading (although we note that permeability increased slightly during the latter stages of deformation) (Figure 7). The porosity and permeability of KT2 both increased during depressurization, and we note that the permeability of KT2 was higher at the end of the experiment than at the start (Figure 7). For KT3, the porosity decreased while the permeability increased slightly during differential stress loading, and porosity and permeability both increased during depressurization (Figure 7). The permeability of KT3\_1\_EPFL was higher, and the permeability of KT3\_3\_EPFL was more-or-less the same, at the end and beginning of the experiment (Figure 7).

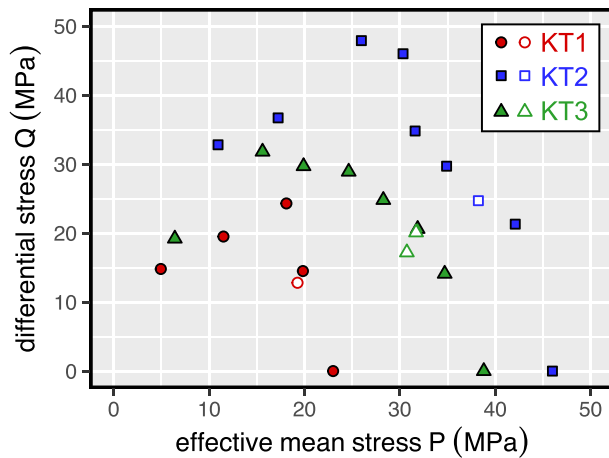


**Figure 5.** Differential stress at failure (the peak stress for the brittle experiments and  $C^*$  for the ductile experiments) as a function of effective mean stress for the three tuffs from Krafla volcano (KT1, KT2, and KT3; data provided in Table 2). Values for  $P^*$  (i.e.,  $Q = 0$  MPa) are also shown. Filled symbols - data from ITES (Strasbourg, France; 20 mm-diameter samples); open symbols - data from EPFL (Switzerland; 37 mm-diameter samples).

were considered the consequence of grain crushing in the case of sandstone, and cataclastic pore collapse in the case of limestone and tuff. Therefore, as observed in other porous tuffs from Campi Flegrei (Heap et al., 2014) and the Alban Hills (Zhu et al., 2011), we consider that the cataclastic collapse of pores and the formation of microcracks at pressures above  $P^*$  can explain the increase in the rate of P-wave velocity decrease per unit pressure (Figure 2a).

An increase in P-wave velocity at large volumetric strains, as seen in KT1 as pressure was increased from 45 to 60 MPa (Figure 2a), has also been observed in porous limestones (Baud et al., 2017; Dautriat et al., 2011). The onset of P-wave velocity increase marks the pressure at which the influence of porosity reduction resulting from pore collapse (acting to increase P-wave velocity) outweighs the influence of the microcracking associated with pore collapse (acting to decrease P-wave velocity). We anticipate that P-wave velocity would also increase in KT2 and KT3, rocks that transition to inelastic behavior at higher pressures, at pressures higher than those used here (i.e., >60 MPa; Figure 2a). During depressurization, the P-wave velocity of all three tuffs decreased (Figure 2a) and can be explained by the progressive opening of microcracks and widening of contacts between fragmented particles within collapsed pores as a function of decreasing effective pressure.

At the onset of inelastic hydrostatic compaction,  $P^*$ , the rate of permeability decrease per unit pressure increased in KT1 and KT3 (Figure 2b). We interpret this increase to be a consequence of cataclastic pore collapse, as previously discussed for porous limestones (Dautriat et al., 2011) and porous tuffs (Heap et al., 2014). Our data also show that the influence of cataclastic pore collapse and microcracking on permeability decreased as a function of the initial permeability (Figure 2b). For example, large decreases in permeability at pressures above  $P^*$  were observed for KT1, moderate decreases were observed for KT3, and the progressive decrease observed for KT2 as a function of increasing effective pressure did not appear to be influenced by  $P^*$  (Figure 2b). Since the decrease in porosity as a function of strain is not dissimilar between the three tuffs (Figures 3d, 3e, and 3f), we consider that the differences in the evolution of permeability following  $P^*$  (Figure 2b) is a result in the relative change in void space tortuosity between the three tuffs. In the high-permeability tuff, KT1, the collapse of pores disturbs the low-tortuosity porosity structure of the sample, and the microcracks that form surrounding the pores do not contribute to decreasing the void space tortuosity. By contrast, in the low-permeability tuff, KT2, the void space is already tortuous and the collapse of pores does not greatly influence the permeability, and the resultant microcracking serves to reduce void space tortuosity by connecting adjacent collapsed pores. An end-member example of this behavior was observed for a porous lava (a trachyandesite from the Azores), the permeability of which increased at pressures above  $P^*$  (Loaiza et al., 2012). In the case of this lava, although hydrostatic inelastic compaction was characterized by a net decrease in porosity, the microcracks that formed between

## 5. Discussion

### 5.1. Influence of Effective Pressure on P-Wave Velocity and Permeability

Our data show that P-wave velocity and permeability increased and decreased, respectively, as effective pressure increased up to a threshold pressure corresponding to  $P^*$  (~25 MPa for KT1, ~45 MPa for KT2, and ~40 MPa for KT3; although we note that the permeability of KT2 decreased steadily as the effective pressure was increased from 1 to 60 MPa, without a pronounced increase in the decrease of permeability as a function of effective pressure) (Figure 2). Increases in P-wave velocity (Fortin et al., 2011; Nara et al., 2011; Stanchits et al., 2006; Vanorio et al., 2002; Vinciguerra et al., 2005, 2009) and decreases in permeability (Fortin et al., 2011; Heap et al., 2014, 2018a, 2022; Loaiza et al., 2012; Nara et al., 2011; Vinciguerra et al., 2005, 2009) have been previously observed during the elastic hydrostatic loading of volcanic rocks, and have been interpreted as due to the closure of pre-existing microcracks or the pinching of narrow pore throats.

At the onset of inelastic hydrostatic compaction,  $P^*$ , the rate of P-wave velocity decrease per unit pressure increased (Figure 2a). Notable decreases in P-wave velocity at pressures higher than  $P^*$  have been previously observed in porous sandstones (Fortin et al., 2005), porous limestones (Baud et al., 2017; Dautriat et al., 2011), and porous tuffs (Heap et al., 2014). These decreases

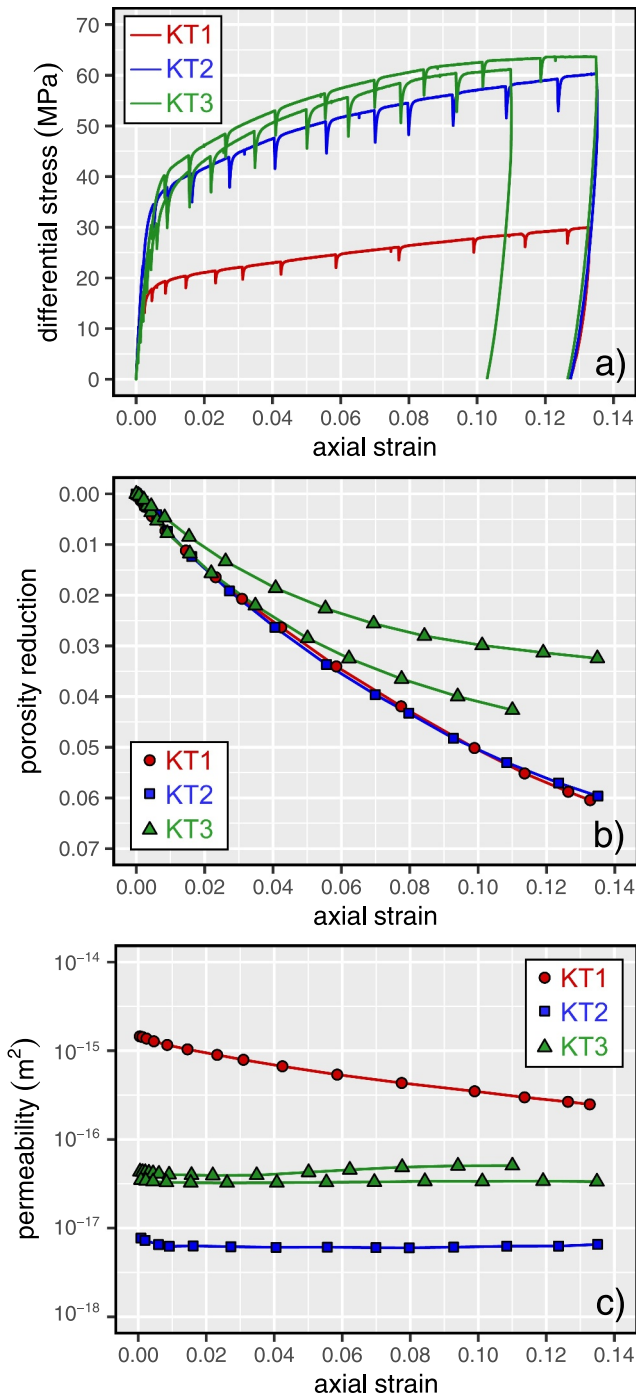


**Figure 6.** (a) Stress-strain curves for the experiments performed on Krafla tuff (KT1, KT2, and KT3) at effective pressure corresponding to the ductile regime (15, 30, and 25 MPa for KT1, KT2, and KT3, respectively) during which permeability was measured during deformation. Stress drops on the stress-strain curve are due to stress relaxation during the measurements of permeability. (b) Porosity reduction as a function of axial strain for the experiments shown in panel (a). (c) Permeability as a function of axial strain for the experiments shown in panel (a). The relative error on our permeability measurements is <1% (i.e., within the symbol size).

adjacent collapsed pores served to decrease void space tortuosity and, therefore, increase the permeability of the sample.

During depressurization, in contrast to the evolution of P-wave velocities (Figure 2a), large changes in permeability were not observed for all three tuffs (Figure 2b). The permeability of KT2 remained more-or-less constant as effective pressure was reduced from 60 to 1 MPa, and the permeability of KT1 and KT3 increased only at effective pressures below ~20 MPa (Figure 2b). Therefore, the increase in microcrack aperture, and the widening of contacts between fragmented particles within collapsed pores, as a function of decreasing effective pressure must not have greatly decreased the tortuosity of the void space in these tuffs from Krafla volcano.

## 5.2. The Mechanical Behavior of Tuff

In this section, we compare our mechanical data with published data for tuff from Campi Flegrei (Aversa & Evangelista, 1998), from Alban Hills (Zhu et al., 2011), from Whakaari volcano (New Zealand; Heap et al., 2015b), and from Mt. Epomeo (Italy; Marmoni et al., 2017; Heap et al., 2018b) (Table 3).

### 5.2.1. The Shape of the Yield Caps: Elliptical or Linear?

The yield caps for porous sedimentary rocks (sandstones and limestones; Wong & Baud, 2012) and tuffs (Heap & Violay, 2021; Wong & Baud, 2012) are elliptical or quasi-elliptical in  $P$ - $Q$  stress space and can be described by (Wong & Baud, 2012; Wong et al., 1997):

$$\frac{(P/P^* - \gamma)^2}{(1 - \gamma)^2} + \frac{(Q/P^*)^2}{(\delta)^2} = 1. \quad (4)$$

For porous sedimentary rocks,  $\gamma$  and  $\delta$  are 0.5 and 0.5–0.7, respectively (Wong & Baud, 2012; Wong et al., 1997). Heap and Violay (2021) showed that porous tuffs also have elliptical yield caps, whereas lavas typically have linear yield caps. To discuss the shape of the yield cap for the tuffs from Krafla, we re-plot their yield caps (those shown in Figure 5), but with the differential stress and effective mean stress normalized to  $P^*$  (Figure 8a). Also plotted on Figure 8a are data for Whakaari tuff and Alban Hills tuff (data for which  $P^*$  is available), and the curves for  $\gamma = 0.5$  and  $\delta = 0.5$  and 0.7 (Equation 4). Therefore, if the data plot within these modeled curves (i.e., within the dark gray zone), the shape of the yield cap is similarly elliptical to those for sandstone (from Wong & Baud, 2012). As can be seen in Figure 8a, much of the data for the tuffs from Krafla plot outside of the modeled curves, indicating that the yield caps show some degree of linearity (as sometimes seen for lavas; Heap & Violay, 2021) when compared to sandstones (the modeled curves) and the tuffs from Whakaari and the Alban Hills. Although the data here suggest that the Krafla tuffs have yield caps that differ in shape to previously measured tuffs (Whakaari and the Alban Hills), especially KT1 and KT2, we suggest that more data are required to make firm conclusions.

### 5.2.2. Stresses Required for Inelastic Behavior During Differential Loading

Experimental studies on porous volcanic (Heap & Violay, 2021) and porous sedimentary (Wong & Baud, 2012) rocks have shown that porosity exerts control on the size of the yield cap, where rocks with a low and high porosity are characterized by yield caps at high and low stresses, respectively. If we

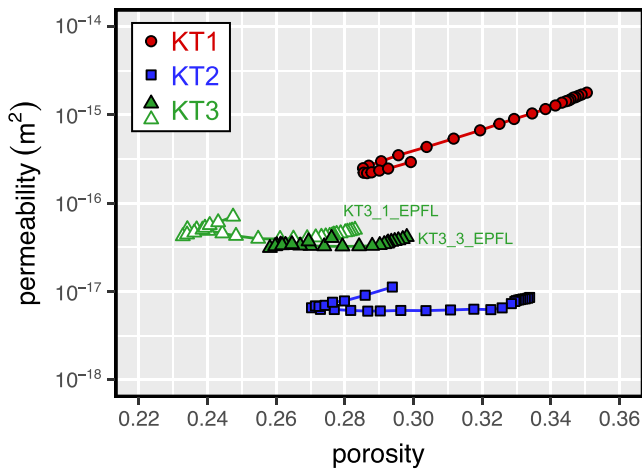


**Figure 7.** Permeability as a function of porosity for the experiments performed on Krafla tuff (KT1, KT2, and KT3) shown in Figure 6. Porosity and permeability are shown for hydrostatic pressurization, differential stress loading, and depressurization. Data for samples KT3\_1\_EPFL and KT3\_3\_EPFL are shown in unfilled and filled triangles, respectively. The relative error on our permeability measurements is <1% (i.e., within the symbol size).

first compare the data for the three tuffs from Krafla (Figure 8b), we notice, however, that the stresses required for inelastic behavior are not the highest for the tuff with the lowest porosity (KT3;  $\phi = 0.29$ ). For the three Krafla tuffs, the lowest stresses are required for KT1 ( $\phi = 0.33$ ), the highest stresses are required for KT2 ( $\phi = 0.33$ ), and the data for KT3 ( $\phi = 0.29$ ) plot at stresses in between KT1 and KT2 (Figure 8b). It is clear from these data that the large range in stresses required for inelastic behavior cannot be explained by their small differences in porosity. When we compare the Krafla data with the published data, we notice that (a) the tuff from Whakaari requires stresses much higher than the three tuffs from Krafla, despite its very similar porosity ( $\phi = 0.29$ ) and (b) the tuff from Campi Flegrei requires stresses similar to KT1, despite its much higher porosity ( $\phi = 0.45$ – $0.5$ ) (Figure 8b). We can conclude, for the tuffs shown in Figure 8b, that there must be factors other than porosity controlling the stress required for inelastic behavior.

Other factors known to influence the size of the yield cap of granular material are grain size (Carbillet et al., 2021) and grain size distribution (Carbillet et al., 2022). Smaller grains and a narrower grain size distributions create granular materials that transition to inelastic behavior at higher stresses (Carbillet et al., 2021, 2022). In terms of grain size, KT2 and KT3 have a similar mean grain size of  $\sim 44$ – $45 \mu\text{m}$ , and KT1 not only contains larger fragments, but also has a larger matrix mean grain size of  $\sim 73 \mu\text{m}$  (Figures S1, S2, and S3 in Supporting Information S1). Therefore, the fact that KT1 transitions to inelastic

behavior at lower stresses than KT2 and KT3 (Figure 8b) could, in part, be explained by its larger grain size. However, KT2 and KT3 have similar mean grain sizes and require different stresses for inelastic behavior (Figure 8b). In terms of grain size distribution, the tuff that requires the highest stresses for inelastic behavior, KT2, also has the narrowest grain size distribution (standard deviation of  $\sim 22 \mu\text{m}$ ) and, therefore, could explain, in part, the high stresses required for inelastic behavior in KT2. Although the high heterogeneity of KT1 could explain its relative weakness, we note that the grain size distribution of the matrix is wider in KT3 than KT1 (Figures S1, S2, and S3 in Supporting Information S1). When we compare the Krafla tuff data with those already published, we find that (a) the tuff from Whakaari, which requires very high stresses for inelastic behavior (Figure 8b), not only has a similar grain size and grain size distribution to KT2 and KT3 (Heap et al., 2015b), but it is also similarly homogeneous on the sample scale and (b) the yield cap for KT3 is similar to that for the Alban Hills tuff (Figure 8b), which is not only more porous, but is also heterogenous on the microscale and sample scale and is characterized by a large average grain size and a wide grain size distribution (Zhu et al., 2011). These comparisons suggest that there is a parameter other than porosity, grain size, and grain size distribution that is influencing the mechanical behavior of the tuffs.

The final factor to consider is the mineral composition of the tuffs and, in particular, the presence of sheet phyllosilicates (clay minerals and chlorite) and zeolites (Table 1). Sheet phyllosilicates such as clay minerals and

**Table 3**  
Tuff Descriptions

Volcano	Porosity	Description	References
Campi Flegrei (Italy)	0.45–0.50	Fine-grained and homogenous; small pore size (50% of the void space by volume is connected by pore throats with a radius $< 1 \mu\text{m}$ )	Aversa and Evangelista (1998)
Alban Hills (Italy) (Tufo del Palatino unit)	0.32	Heterogenous matrix-supported rock that contains mm-to-cm-sized angular lithic fragments and porous lapilli; double porosity consisting of macro- ( $\sim 100 \mu\text{m}$ ) and micropores ( $\sim 10 \mu\text{m}$ )	Zhu et al. (2011)
Whakaari volcano (New Zealand) (block WI21)	0.29	Fine-grained and homogenous; typical pore size of $\sim 50$ – $100 \mu\text{m}$ ; consists mostly of devitrified shards of glass, now hydrated amorphous silica (opal-A), and alunite	Heap et al. (2015b)
Mt. Epomeo (Italy)	0.45	Extremely heterogeneous matrix-supported rock that contains angular lithic fragments and porous lapilli up to 20 mm in diameter within an altered clay- and zeolite-rich matrix; pores range from several tens of $\mu\text{m}$ up to several mm	Marmoni et al. (2017); Heap et al. (2018b)

*Note.* Source volcano, porosity, and textural descriptions for four tuffs for which mechanical data exist for comparison.

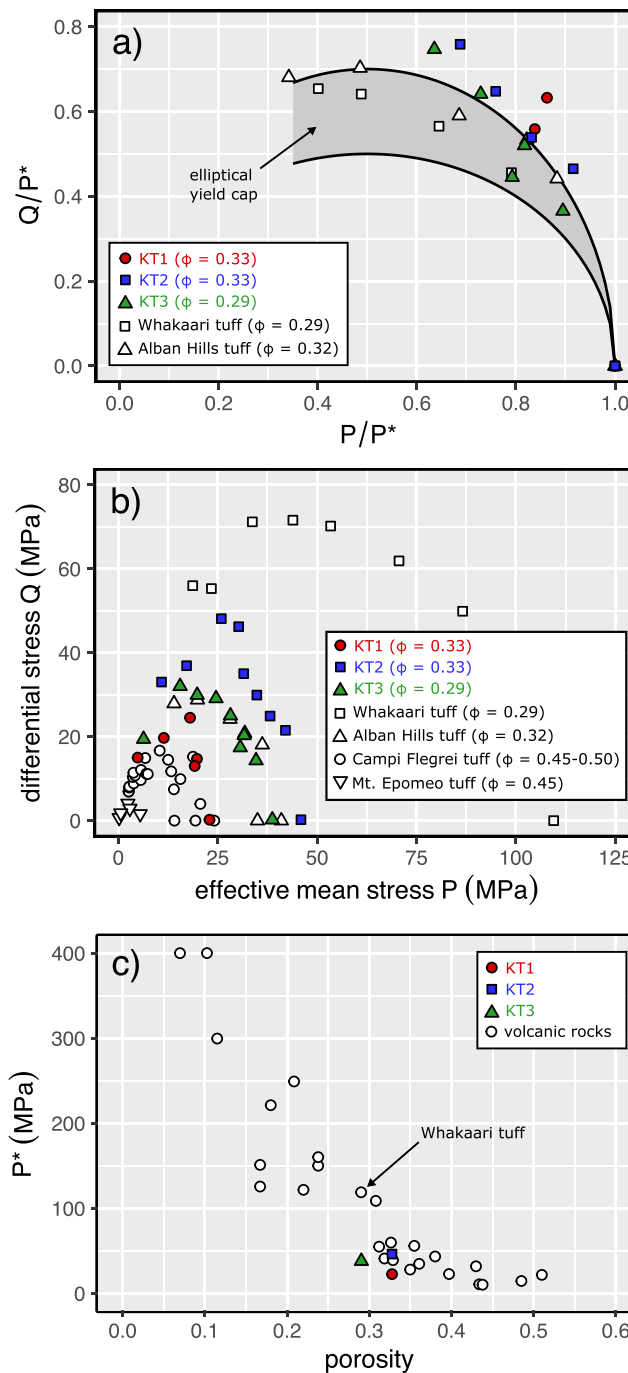


**Figure 8.** (a) Differential stress as a function of effective mean pressure for the three tuffs from Krafla (KT1, KT2, and KT3), both normalized to  $P^*$ . Also shown are data for tuff from Alban Hills (Italy; Zhu et al., 2011) and Whakaari (New Zealand; Heap et al., 2015b). The two curves represent idealized elliptical yield caps (Equation 4), assuming  $\delta = 0.5$  and  $0.7$  and  $\gamma = 0.5$  (see text for details). (b) Differential stress at failure as a function of effective mean stress for the three tuffs from Krafla (KT1, KT2, and KT3), alongside data for tuff from Campi Flegrei (Italy; Aversa & Evangelista, 1998), Alban Hills (Italy; Zhu et al., 2011), Whakaari (New Zealand; Heap et al., 2015b), and Mt. Epomeo (Italy; Marmoni et al., 2017). The porosities of the rocks,  $\phi$ , are provided in the legend. (c)  $P^*$  as a function of porosity for a range of volcanic rocks (data from this study; Adelinet et al., 2013; Eggertsson et al., 2020b; Heap et al., 2014, 2015a, 2015b, 2016; Heap & Violay, 2021; Loaiza et al., 2012; Lockner & Morrow, 2008; Marmoni et al., 2017; Shimada, 2000; Zhu et al., 2011).



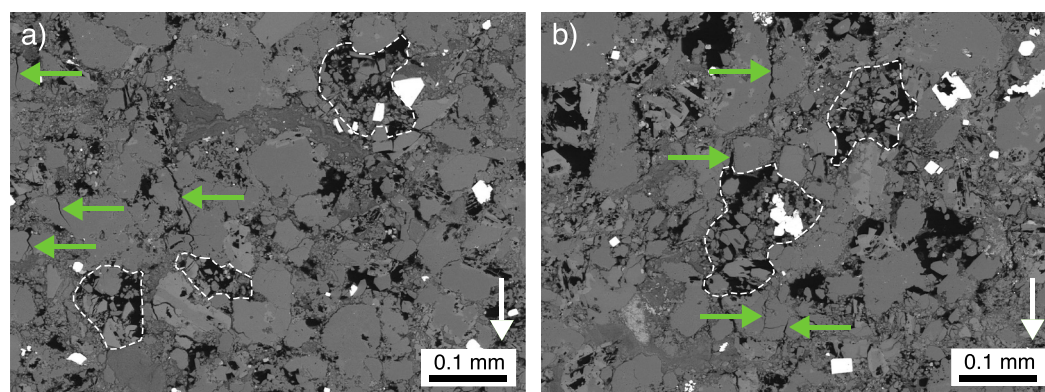


**Figure 9.** Backscattered scanning electron microscope (SEM) images of the tuff from Krafla deformed in the ductile regime ( $P_c$  of 30 MPa). Examples of collapsed pores are delineated by dashed white lines, the green arrows point to microcracks, and the white arrows indicate the loading direction (also the direction of fluid flow).

chlorite are well-known to be frictionally weak minerals (e.g., Behnsen & Faulkner, 2012; Ikari et al., 2009). Further, clay minerals and zeolites are also considered to reduce the strength of tuff in the presence of water (Heap et al., 2018c) and chlorite, another mineral found in the tuffs from Krafla (Table 1), was found to greatly reduce the uniaxial compressive strength of sandstone in the presence of water (Heap et al., 2020b). Indeed, the coefficient of friction of clay minerals and chlorite is lowered (e.g., Behnsen & Faulkner, 2012), and the fracture toughness ( $K_{IC}$ ) of rocks containing clay minerals (Nara et al., 2012; Noël et al., 2021b) is reduced, in the presence of water. We highlight that KT1, the weakest of the three tuffs from Krafla, contains the most clay minerals and chlorite (27.3 wt% of interlayered chlorite-smectite; Table 1). The total sum of clay minerals and chlorite in KT2 and KT3 are, however, reasonably similar (KT2 contains 20.9 wt% of interlayered chlorite-smectite and KT3 contains 15 wt% of R3 illite-smectite and 2.8 wt% of chlorite; Table 1). The influence of mineral composition on the mechanical behavior of tuff is further emphasized when we compare our data with those previously published: (a) the relatively strong tuff from Whakaari (which is similar to KT3 in terms of porosity, grain size, and grain size distribution) does not contain any clay minerals, chlorite, or zeolites (block WI21; Heap et al., 2015b) and (b) the more porous and more heterogeneous tuff from Alban Hills, which has a similar yield cap to KT3, only contains zeolites (Palladino et al., 2001; Zhu et al., 2011). We conclude that the mechanical behavior of tuff is greatly influenced by the presence of sheet phyllosilicates (clay minerals and chlorite) and zeolites, and that other factors, such as porosity, grain size, and grain size distribution, also play a contributing role. The relative weakness of Krafla tuff is discussed in more detail below using micromechanical models.

### 5.2.3. Pressures Required for Inelastic Behavior Under Hydrostatic Conditions

The values of  $P^*$  for the three tuffs from Krafla are plotted as a function of porosity alongside compiled data for volcanic rocks (lavas and tuffs) in Figure 8c. This compilation shows that  $P^*$  decreases significantly (from  $\sim 400$  to  $\sim 50$  MPa) and almost linearly in volcanic rocks as porosity is increased to  $\sim 0.3$ . At porosities above  $\sim 0.3$ , the decrease in  $P^*$  as a function of increasing porosity is more gradual (Figure 8c). These observations are similar to those made for a variably porous limestone (Baud et al., 2017). The tuffs from Krafla, which have a porosity of  $\sim 0.29$ – $0.3$ , are at the intersection of these regimes (Figure 8c). The differences in the onset of hydrostatic inelastic compaction in tuff can be explained by the rationale outlined in the above subsection. For example, the high  $P^*$  of Whakaari tuff ( $P^* = 109.5$  MPa) compared to KT2 and KT3 ( $P^* = 46$  and  $38.8$  MPa, respectively) (Figure 8c), tuffs with similar physical characteristics, is likely the result of the presence of sheet phyllosilicates (clay minerals and chlorite) and zeolites in the Krafla tuffs (minerals not present in the tuff from Whakaari).

### 5.2.4. Inelastic Behavior in Tuffs: Insights From Micromechanical Modeling

Zhu et al. (2011) combined the pore-crack model of Sammis and Ashby (1986) and the stresses needed to yield a macropore within an effective medium (using the Mohr-Coulomb failure criterion) to study how micropores affect the onset of inelastic hydrostatic compaction,  $P^*$ , in porous tuff:

$$P^* = \frac{0.883}{\phi^{0.414}} S^*, \quad (5)$$

where

$$S^* = \frac{K_{IC}}{(\phi_*/\phi)^{0.414} \sqrt{\pi a^*}}. \quad (6)$$

where  $\phi_*$  and  $a^*$  are the porosity of the effective medium and the average micropore radius, respectively. The parameter  $S^*$  encapsulates the combined influence of the partitioning of micro- and macroporosity, the micropore radius, and the fracture toughness (Zhu et al., 2011). To better understand the influence of mineral composition on the mechanical behavior of tuff, we will compare two tuffs with similar physical characteristics (porosity, grain size, and pore size) that (a) contain no clay minerals, chlorite, or zeolites (Whakaari tuff; Heap et al., 2015b) and (b) abundant clay minerals, chlorite, and zeolites (tuff KT3 from Krafla; 15 wt% of R3 illite-smectite, 2.8 wt% of chlorite, and 6.7 wt% of wairakite; Table 1). For KT3,  $S^*$  is 25.8 MPa. Following previous studies (Zhu et al., 2010), we quantified the proportion of macropores in KT3 with an equivalent diameter  $>33 \mu\text{m}$  using SEM images and found that it represents a macroporosity of 0.03, and in turn a ratio  $(\phi_*/\phi)$  of 0.9. Although we do not have direct measurements of  $K_{IC}$ , this parameter can be estimated using UCS measurements following the pore-crack model of Sammis and Ashby (1986) and the analytical approximation provided by Zhu et al. (2010):

$$UCS = \frac{1.325 K_{IC}}{\phi^{0.414} \sqrt{\pi r}}. \quad (7)$$

For KT3, we measured UCS values of 32.3 and 19.2 MPa in nominally dry and water-saturated conditions, respectively (Table 2). At a relatively high porosity ( $\phi > 0.25$ ), Equation 7 predicts that the UCS is mostly controlled by the average pore size. In a dual porosity medium, Baud et al. (2017) showed that the pore size inferred from the pore crack model is typically in the range of the larger macropores. Based on our microstructural observations, we fixed this radius at  $60 \mu\text{m}$ , which leads to  $K_{IC}$  values of 0.2 and 0.11  $\text{MPa}\cdot\text{m}^{1/2}$  for dry and wet KT3, respectively. The calculated weakening effect of water is consistent with data reported on tuff (Zhu et al., 2011) and sandstones (Noël et al., 2021b). Based on the above values, the predicted micropore size in KT3 using Equation 6 is  $a^* = 7 \mu\text{m}$ .

These damage mechanics models can also help analyze the observed differences in strength between the tuff from Whakaari and KT3. From the microstructural data of Heap et al. (2015b), we infer the same partitioning between macro- and micropores as for the tuff from Krafla (i.e.,  $\phi_*/\phi = 0.9$ ) and comparable macropore sizes. The water-saturated UCS of Whakaari tuff is 56 MPa leading to  $UCS_{kr}/UCS_{wh} = P_{kr}^*/P_{wh}^* = 0.34$  (where  $UCS_{kr}$  and  $P_{kr}^*$ , and  $UCS_{wh}$  and  $P_{wh}^*$ , are the UCS and  $P^*$  for KT3 and Whakaari tuff, respectively). For Whakaari tuff, we infer a value of  $K_{IC}$  of  $\sim 0.3 \text{ MPa}\cdot\text{m}^{0.5}$  and an identical micropore size  $a^*$  of  $7 \mu\text{m}$ . The models therefore suggest that KT3 is significantly weaker than Whakaari tuff because of a smaller value of  $K_{IC}$  which, in the absence of significant microstructural differences, is likely due to the presence of sheet phyllosilicates (clay minerals and chlorite) and zeolites in KT3 (see also Nara et al., 2012). For example, Nara et al. (2012) showed that the  $K_{IC}$  of sandstone containing smectite was reduced as a function of increasing relative humidity: the expansion of smectite (i.e., an increase in basal spacings) in the presence of water increases the ease at which microcracks can propagate. An alternative way to explain these data using the models implies that the macro- and micropores are almost an order of magnitude smaller in Whakaari tuff, which is in disagreement with microstructural observations.

### 5.3. Influence of Deformation in the Ductile Regime on Permeability

#### 5.3.1. The Evolution of Permeability in Tuff: The Influence of Initial Microstructure

The permeability of KT1 decreased continuously up to the maximum axial strain whereas, although the change in permeability was not large, the permeability of KT2 and KT3 first decreased and then increased (Figures 6 and 7). An increase in the permeability of the tuff during deformation in the ductile regime can be considered surprising, because the available published data of the same type have shown that the permeability of porous sandstone (Baud et al., 2012; Fortin et al., 2005; Zhu & Wong, 1997), porous limestone (Meng et al., 2019), welded tuff (Alam

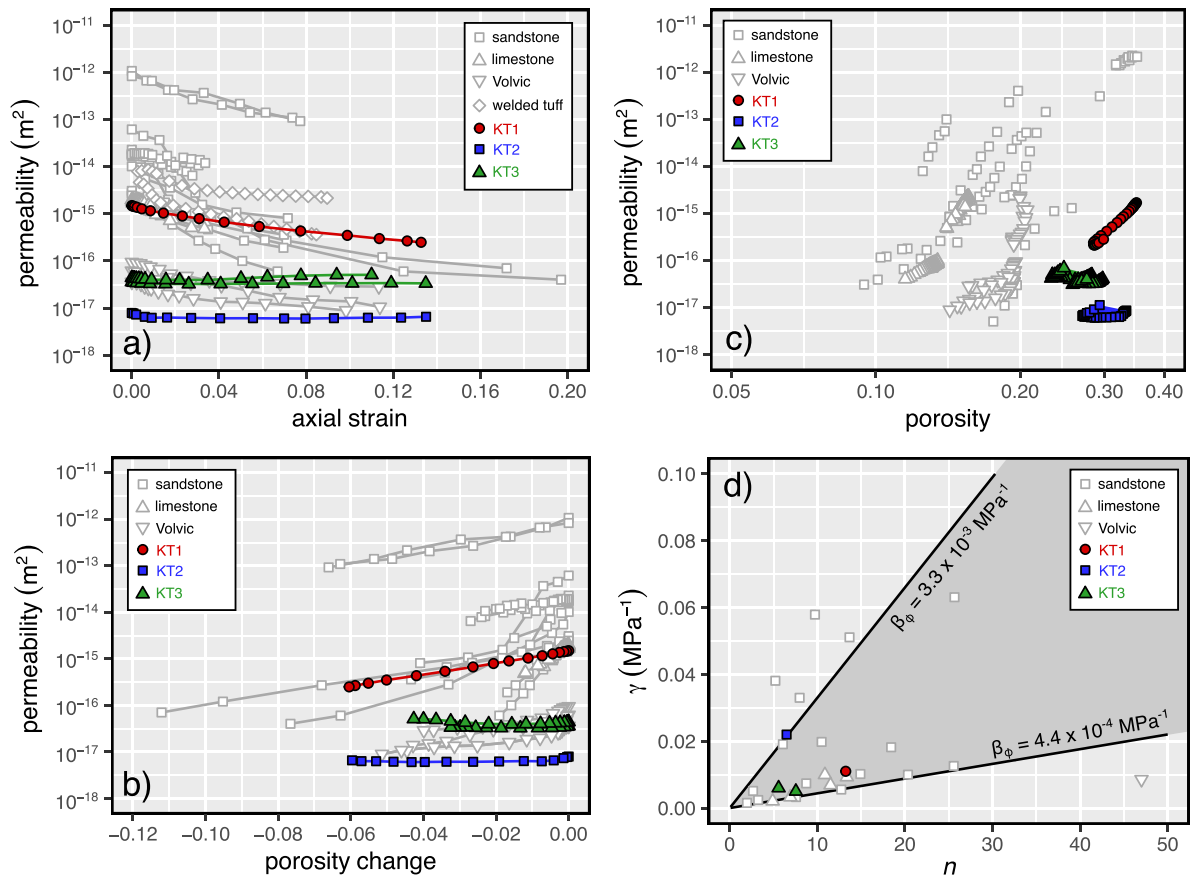


**Figure 10.** Permeability as a function of axial strain (a) and porosity change (b) for Krafla tuff (KT1, KT2, and KT3) in the ductile regime. Also shown are available data for Volvic trachyandesite (white upside-down triangles; Heap et al., 2022), welded tuff (white diamonds; Alam et al., 2014), limestones (white triangles; Meng et al., 2019), and sandstones (white squares; Baud et al., 2012; Fortin et al., 2005; Zhu & Wong, 1997). (c) Permeability as a function of porosity for elastic and inelastic data for Krafla tuff (KT1, KT2, and KT3) in the ductile regime during hydrostatic and triaxial deformation experiments. Also shown are elastic and inelastic data for Volvic trachyandesite during hydrostatic and triaxial deformation experiments (Heap et al., 2022) (white upside-down triangles), porous limestones during triaxial deformation experiments (Meng et al., 2019) (white triangles), and porous sandstones during hydrostatic experiments (David et al., 1994) (white squares). (d) Pressure sensitivity coefficient,  $\gamma$ , as a function of porosity sensitive parameter,  $n$ , for Krafla tuff (KT1, KT2, and KT3) and compiled data for Volvic trachyandesite (Heap et al., 2022) (white upside-down triangles), limestones (white triangles; Meng et al., 2019), and sandstones (white squares; David et al., 1994; Yale, 1984). All data are for the elastic regime (hydrostatic data and data collected prior to  $C^*$  during differential loading).

et al., 2014), and porous lava (Heap et al., 2022) decreased as a function of axial strain (Figure 10a) and porosity loss (Figure 10b) in the ductile regime.

For KT1, the tuff with the highest permeability ( $\sim 10^{-15} \text{ m}^2$ ), the loss in permeability as a function of axial strain and porosity loss is similar to that previously observed for other porous rocks, including the high-permeability ( $\sim 10^{-14} \text{ m}^2$ ) welded tuff from Shikotsu (Figures 10a and 10b). As discussed in Alam et al. (2014), we interpret this permeability reduction during deformation in the ductile regime to be due to the cataclastic collapse of pores which, in these high-permeability tuffs with low-tortuosity pore structures, is able to increase void space tortuosity, and therefore decrease permeability. By contrast, the initial porosity structure of KT2 and KT3 is tortuous: these samples are characterized by high porosities ( $\sim 0.28\text{--}0.34$ ) and low permeabilities ( $\sim 10^{-18}\text{--}10^{-17} \text{ m}^2$ ). We interpret the initial small decrease in permeability in KT2 and KT3 to be the result of the cataclastic collapse of pores but, because the void space is already tortuous, pore collapse does not greatly influence the void space tortuosity and therefore permeability.

To investigate why the permeability KT2 and KT3 then increased following further deformation in the ductile regime (Figures 6, 7, and 10), we performed microstructural analysis on samples of KT3 deformed in the ductile regime (Figure 9). Figure 9 first confirms that the microstructural mechanism of deformation in the tuffs from Krafla in the ductile regime is cataclastic pore collapse (delineated by dashed white lines in Figure 9), as observed

previously for porous tuffs (Heap et al., 2014, 2015b; Zhu et al., 2011). However, we also note the presence of axially orientated microcracks (i.e., in the direction of loading) surrounding some of the collapsed pores (marked by the green arrows in Figure 9). Collapsed pores in deformed porous rocks are very often bounded by microcracks (Heap & Violay, 2021; Wong & Baud, 2012).

Based on our microstructural observations (Figure 9), we propose that the increase in permeability during the ductile deformation of KT2 and KT3 is the result of a decrease in void space tortuosity as the microcracks surrounding collapsed pores connect adjacent pores. Therefore, although porosity is decreasing, void space tortuosity is decreasing, resulting in an increase in permeability. We note that these microcracks are preferentially axially oriented (i.e., parallel to the sample axis and the imposed pore pressure gradient), which may explain why permeability increases are possible during differential loading (Figures 6 and 7) but not during hydrostatic pressurization (Figure 2b). During differential loading, microcracks form in the direction of the maximum principal stress, as shown in Figure 9, which connect adjacent pores in the direction of fluid flow. By contrast, during hydrostatic pressurization, the microcracks that form surrounding collapsed pores should not have a preferred orientation, and so any connections made between adjacent pores would not necessarily align with the direction of fluid flow. If true, this would imply that, although we measured an increase in permeability during differential loading parallel to the sample axis (i.e., parallel to the maximum principal stress), permeability is likely decreasing in all other directions during differential stress loading, creating a permeability anisotropy. An alternate explanation is that decreases in tortuosity and therefore increases in permeability would be observed under hydrostatic conditions at higher pressures. However, we note that the porosity reduction in the deformation experiments ( $\sim 0.03$ – $0.06$ ; Figure 6b) is not too dissimilar to that expected during hydrostatic pressurization up to 60 MPa (see the hydrostat on Figure 4). Finally, we interpret the increase in permeability during depressurization (Figure 7) to be due to the increase in the aperture of the axially orientated microcracks that formed surrounding collapsed pores (Figure 9). The fact that these microcracks are axially oriented (i.e., in the direction of the imposed pore pressure gradient) explains why permeability increased during depressurization following differential loading (Figure 7), but did not increase significantly during depressurization following hydrostatic pressurization to pressures above  $P^*$  (Figure 2b).

Taken together, the data suggest that initial rock microstructure, and especially the void space tortuosity, exerts a strong influence on the evolution of the permeability of tuff as a function of axial strain in the ductile regime. If the tuff has a low-tortuosity porosity structure and has a high initial permeability, then deformation in the ductile regime will likely reduce permeability, whereas deformation can increase the permeability of relatively low-permeability tuff with a more tortuous porosity structure. These data highlight that more experiments are now required to better understand the influence of initial microstructure on the evolution of permeability in volcanic rocks.

### 5.3.2. Porosity- and Pressure-Dependence of Permeability

We plot permeability as a function of porosity for the three tuffs from Krafla, Volvic trachyandesite (Heap et al., 2022), and porous sedimentary rocks (sandstones and limestones; David et al., 1994; Meng et al., 2019) in Figure 10c. It is common to consider a power-law description for the porosity-dependence of permeability  $k(\phi)$ , where  $k_0$  is a reference permeability (the permeability at  $\phi = \phi_0$ ),  $n$  is a power law exponent (the percolation transport exponent), and  $\phi$  and  $\phi_0$  are the porosity and a reference porosity (the initial value of porosity), respectively:

$$k = k_0 \left( \frac{\phi}{\phi_0} \right)^n \quad (8)$$

In the elastic regime, the values of  $n$  for KT1 and KT2 are 13.24 and 6.49, respectively, and the values of  $n$  for the two KT3 samples are 5.58 and 7.55. These values are much lower than the exponent for Volvic trachyandesite ( $n = 47$ ), but are in the range for porous sandstones and limestones, for which  $n = \sim 2$ – $26$  (Figure 10c). The values of  $n$  for KT2 and KT3 can be considered low when compared to the exponents for other rocks (Figure 10c). We consider the low exponents for KT2 and KT3 to be a consequence of a pore structure that contains abundant, small-diameter pores that are tortuously connected (the permeability of KT2 and KT3 are low, despite their relatively high porosity). Therefore, elastically closing some of the pores and pore throats does not greatly influence the tortuosity of the pore network and, as a result, does not greatly influence permeability. As discussed

above, we consider that KT1, which has a much higher initial permeability than KT2 and KT3, has a low-tortuosity porosity structure. By contrast to KT2 and KT3, the void space tortuosity of KT1, and therefore the permeability, can be influenced by the elastic closure of pores and pore throats, explaining the higher value of  $n$  ( $\sim 13$  compared to  $\sim 6$ – $8$ ; Figure 10c). At stresses above  $C^*$  in the ductile regime (i.e., inelastic deformation), the  $n$  of sandstone and Volvic trachyandesite decreases, but remains constant (i.e.,  $n$  is the same below and above  $C^*$ ) for limestone (Figure 10c). However, while the  $n$  for KT1 decreases at stresses above  $C^*$ , values of  $n$  for KT2 and KT3 first decrease and then become negative (when permeability starts to increase). We highlight that, for all of the other rocks tested (Figure 10c),  $n$  never becomes negative. As discussed above, we consider that this is the result of a decrease in void space tortuosity as axially oriented microcracks form surrounding collapsed pores in response to the differential loading (Figure 9). The low  $n$  for KT2 and KT3, and the increase in permeability during ductile deformation, results in a very small net change in permeability of these tuffs compared to other porous rocks (sandstones, limestones, and porous lava; Figure 10c).

The relationship between permeability,  $k$ , and the effective mean stress,  $P$ , has been considered in terms of an exponential relationship (David et al., 1994):

$$k = k_0 \exp(-\gamma(P - P_0)), \quad (9)$$

where  $\gamma$  is the compression coefficient and  $P_0$  is the effective pressure at the reference permeability  $k_0$ . In the elastic regime, the data for KT1 and KT2 are characterized by  $\gamma = 0.011$  and  $0.022 \text{ MPa}^{-1}$ , respectively, and the values of  $\gamma$  for the two KT3 samples are  $0.006$  and  $0.005 \text{ MPa}^{-1}$ . As discussed in David et al. (1994), Equations 8 and 9 imply a relationship between  $n$  and  $\gamma$  via the pore compressibility  $\beta_\phi$ :

$$\gamma = -\frac{n}{\phi} \frac{d\phi}{dP} = n\beta_\phi. \quad (10)$$

We plot the values of  $n$  and  $\gamma$  for KT1, KT2, and KT3 in Figure 10d, alongside data for Volvic trachyandesite (Heap et al., 2022), limestones (Meng et al., 2019), and sandstones (David et al., 1994; Yale, 1984). We also provide the range of  $\beta_\phi$  ( $4.4 \times 10^{-4}$  and  $3.3 \times 10^{-3} \text{ MPa}^{-1}$ ) from David et al. (1994) that brackets the majority of the porous sandstone data in Figure 10d (i.e., within the dark gray zone). The data for the Krafla tuffs plot within this range, indicating that the compliance of the pore space in these tuffs from Krafla in the elastic regime is similar to porous sandstones and limestones, and very different to that of Volvic trachyandesite (Figure 10d).

## 6. Implications and Conclusions

Our experiments have revealed the following. (a) Tuff containing sheet phyllosilicates (clay minerals and chlorite) and zeolites are likely mechanically weaker than those without (Figure 8b), and that micromechanical modeling suggests that this is the result of a lower fracture toughness. (b) The permeability of tuff decreases during hydrostatic pressurization, and larger decreases in permeability following  $P^*$  are observed for tuffs that are initially more permeable (Figure 2b). Decreases in permeability during pressurization above  $P^*$  are interpreted as the result of the cataclastic collapse of pores. (c) The evolution of the permeability of tuff during differential loading in the ductile regime depends on microstructure, and particularly the initial void space tortuosity. If the tuff has a low-tortuosity porosity structure and has a high initial permeability, then deformation in the ductile regime will likely reduce permeability, whereas deformation will not appreciably change (and can even increase) the permeability of relatively low-permeability tuff with a more tortuous porosity structure. For initially high permeability tuffs, deformation in the ductile regime results in the cataclastic collapse of pores that can disrupt the porosity structure, increasing tortuosity and therefore decreasing permeability. For initially low permeability tuffs, the cataclastic collapse of pores does not particularly influence the already tortuous porosity structure, and microcracks that form surrounding collapsed pores align to the maximum principal stress, which is also the direction of the pore pressure gradient (i.e., the direction of fluid flow). Therefore, although porosity decreases, void space tortuosity can decrease and permeability can increase during the ductile deformation of initially low permeability tuffs. We will now outline some of the general implications of these findings for volcanic structures and geothermal reservoirs, before discussing some potential implications for Krafla volcano.

The presence of mixed-layer chlorite-smectite in KT1 and KT2 and R3 illite-smectite and chlorite in KT3 suggests that, despite their different depths, (394.0–394.5, 505.5–506.0, and 688.9–690.6 m for KT1, KT2, and

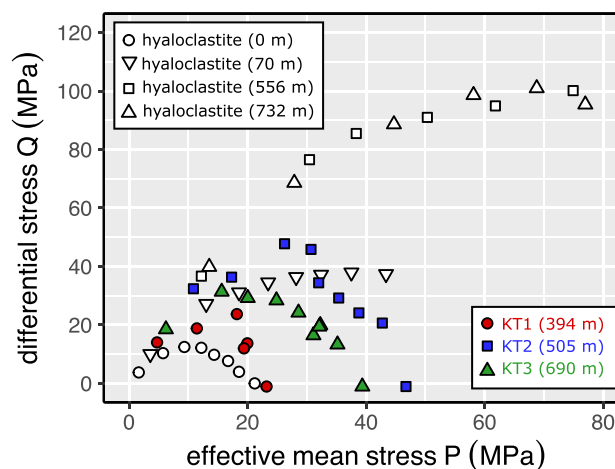


**Figure 11.** Differential stress at failure (the peak stress for the brittle experiments and  $C^*$  for the ductile experiments) as a function of effective mean stress for the three tuffs from Krafla (KT1, KT2, and KT3; data in Table 2) and hyaloclastites (Eggertsson et al., 2020b; open symbols) from Krafla volcano. The depths of the rocks are provided in the legends.

KT3, respectively), all three tuffs are from the mixed-layer alteration zone between the smectite and chlorite zones, at a temperature of  $\sim 160\text{--}270^\circ\text{C}$  (Deer et al., 2004; Escobedo et al., 2021; Kristmannsdóttir, 1979; Utada, 2001). However, KT1 and KT2, the two tuffs from the shallowest depth, also contain epidote and in part amphibole, suggesting that they could exist within the, usually deeper, chlorite-epidote alteration zone (e.g., Escobedo et al., 2021). Epidote can be found in hydrothermal systems below  $200^\circ\text{C}$ , but is more common at slightly higher temperatures of  $\sim 230\text{--}260^\circ\text{C}$  (Bird & Spieler, 2004). From our data, we can conclude that the distribution of alteration minerals within the tuffs at Krafla volcano is complex, with variations in mineral assemblages likely driven by local variations in temperature, or possibly even protolith and fluid compositions. Our mechanical data therefore suggest that tuffs found within the low-temperature ( $<250^\circ\text{C}$ ) alteration zones that characterize shallow hydrothermal systems (Beaufort et al., 2021; Escobedo et al., 2021; Inoue, 1995; Kristmannsdóttir, 1979; Wyering et al., 2014) will be weaker than those found within the overlying unaltered zone (the first few hundred meters) or those located far from a hydrothermal system. Therefore, if the hydrothermal system at a given edifice, dome, caldera, or reservoir expands and incorporates unaltered tuffs, these tuffs may be weakened through alteration, which may result in subsidence and/or instability (Darmawan et al., 2022; Harnett et al., 2022; Harnett & Heap, 2021; Heap et al., 2021b). However, although we can conclude that tuffs within the low-temperature ( $<250^\circ\text{C}$ ) part of a hydrothermal system are likely weaker than tuff above or far from the hydrothermal system, data for tuffs characterized by higher-temperature alteration (i.e., those that contain only chlorite and epidote and no R3 illite-smectite or mixed-layer chlorite-smectite) are not yet available. Therefore, with the available data, it is not possible to state whether tuffs that contain chlorite and epidote, but no R3 illite-smectite or mixed-layer chlorite-smectite, are stronger or weaker than those with the low-temperature ( $<250^\circ\text{C}$ ) alteration assemblage investigated here.

We find that permeability decreases during hydrostatic compaction (Figure 2b), especially above the pressure threshold for inelastic compaction but, and depending on the initial microstructure of the tuff, can either decrease or increase during differential loading when deformed to large axial strains in the ductile regime (Figures 6 and 7). As discussed above, increases in permeability during the ductile deformation of porous rocks have not been observed before (Figure 10), and is considered here to be related to differences in initial microstructure and, in particular, initial void space tortuosity. However, although changes in permeability can result in changes in hydrothermal convection and allow pore pressure to build or dissipate, with the attendant consequences for volcanic hazards and geothermal energy exploitation, we note that, compared to other rocks, the permeability of the tuffs measured herein does not change significantly following elastic and inelastic deformation (Figure 10c). If the permeability of tuff layers can remain relatively high, even following deformation resulting in compaction (i.e., even at depth), then they could act, alongside permeable faults and discontinuities, as important layers for the maintenance of hydrothermal convection at volcanic structures (edifices and calderas) and geothermal reservoirs and/or as important pathways for magmatic outgassing.

Relatedly, we also highlight that deformation in the ductile regime was not localized into compaction bands in the three samples of tuff from Krafla (Figure 9), features that can greatly decrease permeability in porous granular materials (e.g., Vajdova et al., 2004). This observation is in accordance with previous experiments performed on tuff (Heap & Violay, 2021; Heap et al., 2015b; Marmoni et al., 2017; Zhu et al., 2011). Porous lavas, however, do form compaction bands in the ductile regime (as reviewed in Heap & Violay, 2021). Heap and Violay (2021) speculated that the absence of compaction bands in tuff was a consequence of their relatively heterogeneous grain size distribution, a factor known to influence compaction band formation in sandstones (Cheung et al., 2012). However, we highlight that the grain size distribution in KT2 and KT3 is relatively narrow (Figures S2 and S3 in Supporting Information S1). It remains unclear why porous lavas form compaction bands and porous tuffs do not.

In terms of Krafla volcano, the shallow hydrothermal system consists of hyaloclastites, lavas, basaltic intrusions, and tuffs (Eggertsson et al., 2020a, 2020b; Escobedo et al., 2021; Lévy et al., 2018; Mortensen et al., 2014; Weaver et al., 2020). Although no mechanical data exist for the lavas and basaltic intrusions, we can compare our mechanical data with those for hyaloclastites from Krafla volcano published in Eggertsson et al. (2020b) (Figure 11). Although the  $P^*$  of surficial hyaloclastite was measured to be  $\sim 22$  MPa,  $P^*$  could not be measured for two hyaloclastites sampled from boreholes KH-04 (depth of 70–76 m) and KH-06 (depths of 556 and 732 m) due to their lower porosity (Eggertsson et al., 2020b; Figure 11). Therefore, although  $P^*$  in the surficial hyaloclastite collected would be at a depth of  $<1$  km, estimations of  $P^*$  from the presented mechanical data for the borehole samples suggest depths of  $\sim 3$  km (for the sample from 70 to 76 m) and  $\sim 6$  km (for the samples from 556 to 732 m), compared to  $\sim 0.75$ – $1.7$  km for the three tuffs studied herein. The effective pressures and differential stresses required for ductile behavior in the borehole hyaloclastite are also much higher than for the tuff (Figure 11). For example, the brittle-ductile transition in the tuffs occurs at an effective pressure of  $\sim 10$ – $20$  MPa, but pressures of  $\sim 40$  and  $\sim 80$  MPa are required for the hyaloclastites (Figure 11). In other words, inelastic behavior is more easily achieved in the tuff (lower pressures and stresses) than in the hyaloclastite.

Considered together, the data shown in Figure 11 suggest that, although volumetrically less important than hyaloclastite and basaltic lavas within the stratigraphy of the caldera-fill, porous tuff (found to occur at regular intervals within the KH-05 and KH-06 boreholes) is the rock type most likely to experience inelastic hydrostatic compaction and inelastic deformation (brittle and ductile), and therefore physical property changes (such as porosity and permeability), at depths relevant for the shallow hydrothermal system. Therefore, changes in effective pressure resulting in compaction could decrease permeability (Figure 2b), and changes in differential stress resulting in compaction could increase permeability in the direction of the maximum principal stress and create a permeability anisotropy (Figures 6 and 7). However, the high porosity and reasonably high permeability (compared to the borehole hyaloclastites (Eggertsson et al., 2020b) and typical values for lava) of the Krafla tuffs, and the relatively minor changes in permeability resulting from elastic and inelastic deformation (the compaction of other porous rocks can decrease permeability by several orders of magnitude; Figure 10), suggest that the layers of tuff within the caldera-fill stratigraphy could play a role, alongside permeable faults and discontinuities, in the maintenance of shallow hydrothermal convection at Krafla volcano. In other words, the tuff layers, the rock type most susceptible to inelastic deformation within the caldera-fill stratigraphy at Krafla volcano will, therefore, not form effective low-permeability barriers following compaction and, as a result, will not impede fluid flow, even if they are deformed significantly or buried to large depths.

### Data Availability Statement

The laboratory data collected for this study can be freely downloaded from the FigShare data repository (Heap et al., 2024). These data are also available in the Microsoft Excel© spreadsheets (Data Sets S1 to S11) that accompany this publication as Supporting Information. Some analysis was performed using open-source image analysis software ImageJ (<https://imagej.net/ij/>) and the figures were prepared using open-source vector drawing program Inkscape (<https://inkscape.org>) and open-source programs RStudio (<https://posit.co/products/open-source/rstudio/>) and ggplot (<https://ggplot2.tidyverse.org>).

## Acknowledgments

This research was supported by two Hubert Curien Partnership (PHC) grants: a Germaine de Staël grant awarded to M. Heap and M. Violay (Grant 47712SB) and a Ulysses grant awarded to M. Heap and C. Harnett (Grant 47199ZM). The Germaine de Staël grant is implemented by the Ministry for Higher Education, Research, and Innovation (MESRI) and the Ministry for Europe and Foreign Affairs (MEAE) in France, and by the State Secretariat for Education, Research, and Innovation (SERI) and the Swiss Academy of Technical Sciences (SATW) in Switzerland. The Ulysses grant is implemented by the MEAE and the Ministry of Higher Education and Research (MESR) in France, and by the Irish Research Council (IRC) in Ireland. This research also benefited from European Research Council Starting Grant BEFINE (ERC-2017-STG), awarded to M. Violay. M. Heap was also supported by ANR grant MYGALE (“Modelling the physical and chemical gradients of hydrothermal alteration for warning systems of flank collapse at explosive volcanoes”; ANR-21-CE49-0010) and a European Research Council Synergy Grant (ERC-ROTTnROCK-101118491). M. Heap acknowledges support from the Institut Universitaire de France (IUF), and A. Kushnir acknowledges the support of the Swiss National Science Foundation (SNSF) Prima grant ReSiDue (PR00P2-201611). Finally, this research was supported by the Interdisciplinary Thematic Institute (ITI) GeoT, part of the 2021–2028 ITI program of the University of Strasbourg, the French National Research Centre (CNRS), and the French National Institute of Health and Medical Research (Inserm). The ITI GeoT was supported by the SFRI-STRAT’US project (ANR-20-SFRI-0012) and by IdEx Unistra (ANR-10-IDEX-0002) under the Investments for the Future (PIA) framework. We thank Bertrand Renaudie and Laurent Gastaldo for preparing the experimental samples, and Gunel Alizada and Sarvar Mammadov for laboratory support. The comments of two reviewers, the associate editor, and the editor helped improve this manuscript.

## References

- Acosta, M., & Violay, M. (2020). Mechanical and hydraulic transport properties of transverse-isotropic Gneiss deformed under deep reservoir stress and pressure conditions. *International Journal of Rock Mechanics and Mining Sciences*, *130*, 104235. <https://doi.org/10.1016/j.ijrmmms.2020.104235>
- Adelinet, M., Fortin, J., Schubnel, A., & Guéguen, Y. (2013). Deformation modes in an Icelandic basalt: From brittle failure to localized deformation bands. *Journal of Volcanology and Geothermal Research*, *255*, 15–25. <https://doi.org/10.1016/j.jvolgeores.2013.01.011>
- Alam, A. B., Nioka, M., Fujii, Y., Fukuda, D., & Kodama, J. I. (2014). Effects of confining pressure on the permeability of three rock types under compression. *International Journal of Rock Mechanics and Mining Sciences*, *65*, 49–61. <https://doi.org/10.1016/j.ijrmmms.2013.11.006>
- Ármannsson, H., Gudmundsson, A., & Steingrímsson, B. S. (1987). Exploration and development of the Krafla geothermal area. *Jökull Journal*, *37*(1), 13–30. <https://doi.org/10.33799/jokull1987.37.013>
- Árnason, K. (2020). New conceptual model for the magma-hydrothermal-tectonic system of Krafla, NE Iceland. *Geosciences*, *10*(1), 34. <https://doi.org/10.3390/geosciences10010034>
- Árnósson, S., Axelsson, G., & Sæmundsson, K. (2008). Geothermal systems in Iceland. *Jökull Journal*, *58*(1), 269–302. <https://doi.org/10.33799/jokull2008.58.269>
- Aversa, S., & Evangelista, A. (1998). The mechanical behaviour of a pyroclastic rock: Yield strength and “destruction” effects. *Rock Mechanics and Rock Engineering*, *31*(1), 25–42. <https://doi.org/10.1007/s006030050007>
- Baghbanan, A., & Jing, L. (2008). Stress effects on permeability in a fractured rock mass with correlated fracture length and aperture. *International Journal of Rock Mechanics and Mining Sciences*, *45*(8), 1320–1334. <https://doi.org/10.1016/j.ijrmmms.2008.01.015>
- Ball, J. L., Taron, J., Reid, M. E., Hurwitz, S., Finn, C., & Bedrosian, P. (2018). Combining multiphase groundwater flow and slope stability models to assess stratovolcano flank collapse in the Cascade Range. *Journal of Geophysical Research: Solid Earth*, *123*(4), 2787–2805. <https://doi.org/10.1002/2017jb015156>
- Baud, P., Exner, U., Lommatsch, M., Reuschlé, T., & Wong, T.-F. (2017). Mechanical behavior, failure mode, and transport properties in a porous carbonate. *Journal of Geophysical Research: Solid Earth*, *122*(9), 7363–7387. <https://doi.org/10.1002/2017jb014060>
- Baud, P., Meredith, P., & Townend, E. (2012). Permeability evolution during triaxial compaction of an anisotropic porous sandstone. *Journal of Geophysical Research*, *117*(B5), B05203. <https://doi.org/10.1029/2012jb009176>
- Bauer, J. F., Krumbholz, M., Luijendijk, E., & Tanner, D. C. (2019). A numerical sensitivity study of how permeability, porosity, geological structure, and hydraulic gradient control the lifetime of a geothermal reservoir. *Solid Earth*, *10*(6), 2115–2135. <https://doi.org/10.5194/se-10-2115-2019>
- Beaufort, D., Papapanagiotou, P., Patrier, P., Fujimoto, K., & Kasai, K. (2021). High temperature smectites in active geothermal systems. In *Water-rock interaction* (pp. 493–496). Routledge.
- Behnen, J., & Faulkner, D. R. (2012). The effect of mineralogy and effective normal stress on frictional strength of sheet silicates. *Journal of Structural Geology*, *42*, 49–61. <https://doi.org/10.1016/j.jsg.2012.06.015>
- Bird, D. K., & Spieler, A. R. (2004). Epidote in geothermal systems. *Reviews in Mineralogy and Geochemistry*, *56*(1), 235–300. <https://doi.org/10.2138/gsrmg.56.1.235>
- Björnsson, A. (1985). Dynamics of crustal rifting in NE Iceland. *Journal of Geophysical Research*, *90*(B12), 10151–10162. <https://doi.org/10.1029/jb090ib12p10151>
- Björnsson, A., Sæmundsson, K., Einarsson, P., Tryggvason, E., & Grönvold, K. (1977). Current rifting episode in north Iceland. *Nature*, *266*(5600), 318–323. <https://doi.org/10.1038/266318a0>
- Blower, J. (2001). Factors controlling permeability–porosity relationships in magma. *Bulletin of Volcanology*, *63*(7), 497–504. <https://doi.org/10.1007/s004450100172>
- Bourbie, T., & Zinsner, B. (1985). Hydraulic and acoustic properties as a function of porosity in Fontainebleau sandstone. *Journal of Geophysical Research*, *90*(B13), 11524–11532. <https://doi.org/10.1029/jb090ib13p11524>
- Brace, W., Walsh, J. B., & Frangos, W. T. (1968). Permeability of granite under high pressure. *Journal of Geophysical Research*, *73*(6), 2225–2236. <https://doi.org/10.1029/jb073i006p02225>
- Cant, J. L., Siratovich, P. A., Cole, J. W., Villeneuve, M. C., & Kennedy, B. M. (2018). Matrix permeability of reservoir rocks, Ngatamariki geothermal field, Taupo volcanic zone, New Zealand. *Geothermal Energy*, *6*(1), 1–28. <https://doi.org/10.1186/s40517-017-0088-6>
- Carbillet, L., Heap, M. J., Baud, P., Wadsworth, F. B., & Reuschlé, T. (2021). Mechanical compaction of crustal analogs made of sintered glass beads: The influence of porosity and grain size. *Journal of Geophysical Research: Solid Earth*, *126*(4), e2020JB021321. <https://doi.org/10.1029/2020jb021321>
- Carbillet, L., Heap, M. J., Baud, P., Wadsworth, F. B., & Reuschlé, T. (2022). The influence of grain size distribution on mechanical compaction and compaction localization in porous rocks. *Journal of Geophysical Research: Solid Earth*, *127*(11), e2022JB025216. <https://doi.org/10.1029/2022jb025216>
- Carlino, S., Piochi, M., Tramelli, A., Mormone, A., Montanaro, C., Scheu, B., & Klaus, M. (2018). Field-scale permeability and temperature of volcanic crust from borehole data: Campi Flegrei, southern Italy. *Journal of Volcanology and Geothermal Research*, *357*, 276–286. <https://doi.org/10.1016/j.jvolgeores.2018.05.003>
- Cheung, C. S., Baud, P., & Wong, T.-F. (2012). Effect of grain size distribution on the development of compaction localization in porous sandstone. *Geophysical Research Letters*, *39*(21), L21302. <https://doi.org/10.1029/2012gl053739>
- Chevalier, L., Collombet, M., & Pinel, V. (2017). Temporal evolution of magma flow and degassing conditions during dome growth, insights from 2D numerical modeling. *Journal of Volcanology and Geothermal Research*, *333*, 116–133. <https://doi.org/10.1016/j.jvolgeores.2017.01.016>
- Collinson, A. S. D., & Neuberg, J. W. (2012). Gas storage, transport and pressure changes in an evolving permeable volcanic edifice. *Journal of Volcanology and Geothermal Research*, *243*, 1–13. <https://doi.org/10.1016/j.jvolgeores.2012.06.027>
- Colombier, M., Wadsworth, F. B., Gurioli, L., Scheu, B., Kueppers, U., Di Muro, A., & Dingwell, D. B. (2017). The evolution of pore connectivity in volcanic rocks. *Earth and Planetary Science Letters*, *462*, 99–109. <https://doi.org/10.1016/j.epsl.2017.01.011>
- Cornelio, C., & Violay, M. (2020). Effect of fluid viscosity on earthquake nucleation. *Geophysical Research Letters*, *47*(12), e2020GL087854. <https://doi.org/10.1029/2020gl087854>
- Darmawan, H., Troll, V. R., Walter, T. R., Deegan, F. M., Geiger, H., Heap, M. J., et al. (2022). Hidden mechanical weaknesses within lava domes provided by buried high-porosity hydrothermal alteration zones. *Scientific Reports*, *12*(1), 1–14. <https://doi.org/10.1038/s41598-022-06765-9>
- Darot, M., & Reuschlé, T. (2000). Acoustic wave velocity and permeability evolution during pressure cycles on a thermally cracked granite. *International Journal of Rock Mechanics and Mining Sciences*, *37*(7), 1019–1026. [https://doi.org/10.1016/s1365-1609\(00\)00034-4](https://doi.org/10.1016/s1365-1609(00)00034-4)
- Dautriat, J., Gland, N., Dimanov, A., & Raphanel, J. (2011). Hydromechanical behavior of heterogeneous carbonate rock under proportional triaxial loadings. *Journal of Geophysical Research*, *116*(B1), B01205. <https://doi.org/10.1029/2009jb000830>



- David, C., Wong, T.-F., Zhu, W., & Zhang, J. (1994). Laboratory measurement of compaction-induced permeability change in porous rocks: Implications for the generation and maintenance of pore pressure excess in the crust. *Pure and Applied Geophysics*, *143*(1), 425–456. <https://doi.org/10.1007/bf00874337>
- Day, S. J. (1996). Hydrothermal pore fluid pressure and the stability of porous, permeable volcanoes. *Geological Society, London, Special Publications*, *110*(1), 77–93. <https://doi.org/10.1144/gsl.sp.1996.110.01.06>
- Deer, W. A., Howie, R. A., & Zussman, J. (2004). *Rock-forming minerals, volume 4B. Framework silicates: Silica minerals, Feldspatoids and the zeolites* (2nd ed., p. 982). The Geological Society.
- Doebelin, N., & Kleeberg, R. (2015). Profex: A graphical user interface for the Rietveld refinement program BGMN. *Journal of Applied Crystallography*, *48*(5), 1573–1580. <https://doi.org/10.1107/s1600576715014685>
- Duquiquet, H., Arbaret, L., Guillou-Frottier, L., Heap, M. J., & Bellanger, M. (2019). On the geothermal potential of crustal fault zones: A case study from the Pontgibaud area (French Massif Central, France). *Geothermal Energy*, *7*(1), 1–29. <https://doi.org/10.1186/s40517-019-0150-7>
- Eggertsson, G. H., Kendrick, J. E., Weaver, J., Wallace, P. A., Utley, J. E., Bedford, J. D., et al. (2020b). Compaction of hyaloclastite from the active geothermal system at Krafla volcano, Iceland. *Geofluids*, *20*, 1–17. <https://doi.org/10.1155/2020/3878503>
- Eggertsson, G. H., Lavallée, Y., Kendrick, J. E., & Markússon, S. H. (2020a). Improving fluid flow in geothermal reservoirs by thermal and mechanical stimulation: The case of Krafla volcano, Iceland. *Journal of Volcanology and Geothermal Research*, *391*, 106351. <https://doi.org/10.1016/j.jvolgeores.2018.04.008>
- Ehrenberg, S. N., & Nadeau, P. H. (2005). Sandstone vs. carbonate petroleum reservoirs: A global perspective on porosity-depth and porosity-permeability relationships. *AAPG Bulletin*, *89*(4), 435–445. <https://doi.org/10.1306/11230404071>
- Eichelberger, J. C., Carrigan, C. R., Westrich, H. R., & Price, R. H. (1986). Non-explosive silicic volcanism. *Nature*, *323*(6089), 598–602. <https://doi.org/10.1038/323598a0>
- Elders, W. A., Friðleifsson, G. Ó., & Albertsson, A. (2014). Drilling into magma and the implications of the Iceland Deep Drilling Project (IDDP) for high-temperature geothermal systems worldwide. *Geothermics*, *49*, 111–118. <https://doi.org/10.1016/j.geothermics.2013.05.001>
- Elsworth, D., & Voight, B. (1996). Evaluation of volcano flank instability triggered by dyke intrusion. *Geological Society, London, Special Publications*, *110*(1), 45–53. <https://doi.org/10.1144/gsl.sp.1996.110.01.03>
- Escobedo, D., Patrier, P., Beaufort, D., Gibert, B., Levy, L., Findling, N., & Mortensen, A. (2021). Contribution of the paragenetic sequence of clay minerals to re-examination of the alteration zoning in the Krafla geothermal system. *Minerals*, *11*(9), 935.
- Farquharson, J., Heap, M. J., Varley, N. R., Baud, P., & Reuschlé, T. (2015). Permeability and porosity relationships of edifice-forming andesites: A combined field and laboratory study. *Journal of Volcanology and Geothermal Research*, *297*, 52–68. <https://doi.org/10.1016/j.jvolgeores.2015.03.016>
- Farquharson, J. I., Baud, P., & Heap, M. J. (2017). Inelastic compaction and permeability evolution in volcanic rock. *Solid Earth*, *8*(2), 561–581. <https://doi.org/10.5194/se-8-561-2017>
- Farquharson, J. I., Heap, M. J., & Baud, P. (2016). Strain-induced permeability increase in volcanic rock. *Geophysical Research Letters*, *43*(22), 11–603. <https://doi.org/10.1002/2016gl071540>
- Fortin, J., Schubnel, A., & Guéguen, Y. (2005). Elastic wave velocities and permeability evolution during compaction of Bleurswiller sandstone. *International Journal of Rock Mechanics and Mining Sciences*, *42*(7–8), 873–889. <https://doi.org/10.1016/j.ijrmms.2005.05.002>
- Fortin, J., Stanchits, S., Vinciguerra, S., & Guéguen, Y. (2011). Influence of thermal and mechanical cracks on permeability and elastic wave velocities in a basalt from Mt. Etna volcano subjected to elevated pressure. *Tectonophysics*, *503*(1–2), 60–74. <https://doi.org/10.1016/j.tecto.2010.09.028>
- Friðleifsson, G. Ó., & Elders, W. A. (2005). The Iceland Deep Drilling Project: A search for deep unconventional geothermal resources. *Geothermics*, *34*(3), 269–285. <https://doi.org/10.1016/j.geothermics.2004.11.004>
- Friðleifsson, G. Ó., Elders, W. A., & Albertsson, A. (2014). The concept of the Iceland deep drilling project. *Geothermics*, *49*, 2–8. <https://doi.org/10.1016/j.geothermics.2013.03.004>
- Gangi, A. F. (1978). Variation of whole and fractured porous rock permeability with confining pressure. *International Journal of Rock Mechanics and Mining Sciences*, *15*(5), 249–257. [https://doi.org/10.1016/0148-9062\(78\)90957-9](https://doi.org/10.1016/0148-9062(78)90957-9)
- Gasperikova, E., Rosenkjaer, G. K., Amason, K., Newman, G. A., & Lindsey, N. J. (2015). Resistivity characterization of the Krafla and Hengill geothermal fields through 3D MT inverse modeling. *Geothermics*, *57*, 246–257. <https://doi.org/10.1016/j.geothermics.2015.06.015>
- Gautason, B., Egilson, T., Anett, B., & Danielsen, P. E. (2007). *Krafla: Borun tveggjakjarnaholna, KH-5 og KH-6 veturinn 2006–2007*. ISOR-07075 (In Icelandic).
- Gudmundsson, A. (2020). *Volcanotectonics: Understanding the structure, deformation and dynamics of volcanoes*. Cambridge University Press.
- Guillou-Frottier, L., Carré, C., Bourguine, B., Bouchot, V., & Genter, A. (2013). Structure of hydrothermal convection in the Upper Rhine Graben as inferred from corrected temperature data and basin-scale numerical models. *Journal of Volcanology and Geothermal Research*, *256*, 29–49. <https://doi.org/10.1016/j.jvolgeores.2013.02.008>
- Harnett, C. E., & Heap, M. J. (2021). Mechanical and topographic factors influencing lava dome growth and collapse. *Journal of Volcanology and Geothermal Research*, *420*, 107398. <https://doi.org/10.1016/j.jvolgeores.2021.107398>
- Harnett, C. E., Heap, M. J., Troll, V. R., Deegan, F. M., & Walter, T. R. (2022). Large-scale lava dome fracturing as a result of concealed weakened zones. *Geology*, *50*(12), 1346–1350. <https://doi.org/10.1130/g50396.1>
- Heap, M., Kushnir, A., Griffiths, L., Wadsworth, F., Marmoni, G. M., Fiorucci, M., et al. (2018b). Fire resistance of the Mt. Epomeo Green Tuff, a widely-used building stone on Ischia Island (Italy). *Volcanica*, *1*(1), 33–48. <https://doi.org/10.30909/vol.01.01.3348>
- Heap, M. J., Baud, P., McBeck, J. A., Renard, F., Carbillet, L., & Hall, S. A. (2020a). Imaging strain localisation in porous andesite using digital volume correlation. *Journal of Volcanology and Geothermal Research*, *404*, 107038. <https://doi.org/10.1016/j.jvolgeores.2020.107038>
- Heap, M. J., Baud, P., Meredith, P. G., Vinciguerra, S., & Reuschlé, T. (2014). The permeability and elastic moduli of tuff from Campi Flegrei, Italy: Implications for ground deformation modelling. *Solid Earth*, *5*(1), 25–44. <https://doi.org/10.5194/se-5-25-2014>
- Heap, M. J., Baumann, T., Gilg, H. A., Kolzenburg, S., Ryan, A. G., Villeneuve, M., et al. (2021a). Hydrothermal alteration can result in pore pressurization and volcano instability. *Geology*, *49*(11), 1348–1352. <https://doi.org/10.1130/g49063.1>
- Heap, M. J., Baumann, T. S., Rosas-Carbajal, M., Komorowski, J. C., Gilg, H. A., Villeneuve, M., et al. (2021b). Alteration-Induced Volcano Instability at La Soufrière de Guadeloupe (Eastern Caribbean). *Journal of Geophysical Research: Solid Earth*, *126*(8), e2021JB022514. <https://doi.org/10.1029/2021jb022514>
- Heap, M. J., Bayramov, K., Meyer, G. G., Violay, M. E. S., Reuschlé, T., Baud, P., et al. (2024). Data for Heap et al. (JGR: Solid Earth) [Dataset]. *FigShare*. <https://doi.org/10.6084/m9.figshare.25359241>
- Heap, M. J., Farquharson, J. I., Baud, P., Lavallée, Y., & Reuschlé, T. (2015a). Fracture and compaction of andesite in a volcanic edifice. *Bulletin of Volcanology*, *77*(6), 1–19. <https://doi.org/10.1007/s00445-015-0938-7>

- Heap, M. J., Farquharson, J. I., Kushnir, A. R., Lavallée, Y., Baud, P., Gilg, H. A., & Reuschlé, T. (2018c). The influence of water on the strength of Neapolitan Yellow Tuff, the most widely used building stone in Naples (Italy). *Bulletin of Volcanology*, *80*(6), 1–15. <https://doi.org/10.1007/s00445-018-1225-1>
- Heap, M. J., Gilg, H. A., Hess, K. U., Mertens, L., Pösges, G., & Reuschlé, T. (2020b). Conservation and restoration of St. George's church (Nördlingen, Germany), a 15th century Gothic church built using suevite from the Ries impact crater. *Journal of Cultural Heritage*, *41*, 256–263. <https://doi.org/10.1016/j.culher.2019.07.002>
- Heap, M. J., & Kennedy, B. M. (2016). Exploring the scale-dependent permeability of fractured andesite. *Earth and Planetary Science Letters*, *447*, 139–150. <https://doi.org/10.1016/j.epsl.2016.05.004>
- Heap, M. J., Kennedy, B. M., Farquharson, J. I., Ashworth, J., Mayer, K., Letham-Brake, M., et al. (2017). A multidisciplinary approach to quantify the permeability of the Whakaari/White Island volcanic hydrothermal system (Taupo Volcanic Zone, New Zealand). *Journal of Volcanology and Geothermal Research*, *332*, 88–108. <https://doi.org/10.1016/j.jvolgeores.2016.12.004>
- Heap, M. J., Kennedy, B. M., Pernin, N., Jacquemard, L., Baud, P., Farquharson, J. I., et al. (2015b). Mechanical behaviour and failure modes in the Whakaari (White Island volcano) hydrothermal system, New Zealand. *Journal of Volcanology and Geothermal Research*, *295*, 26–42. <https://doi.org/10.1016/j.jvolgeores.2015.02.012>
- Heap, M. J., Meyer, G. G., Noël, C., Wadsworth, F. B., Baud, P., & Violay, M. E. (2022). The permeability of porous volcanic rock through the brittle-ductile transition. *Journal of Geophysical Research: Solid Earth*, *127*(6), e2022JB024600. <https://doi.org/10.1029/2022jb024600>
- Heap, M. J., Reuschlé, T., Farquharson, J. I., & Baud, P. (2018a). Permeability of volcanic rocks to gas and water. *Journal of Volcanology and Geothermal Research*, *354*, 29–38. <https://doi.org/10.1016/j.jvolgeores.2018.02.002>
- Heap, M. J., Russell, J. K., & Kennedy, L. A. (2016). Mechanical behaviour of dacite from Mount St. Helens (USA): A link between porosity and lava dome extrusion mechanism (dome or spine)? *Journal of Volcanology and Geothermal Research*, *328*, 159–177. <https://doi.org/10.1016/j.jvolgeores.2016.10.015>
- Heap, M. J., Troll, V. R., Kushnir, A. R., Gilg, H. A., Collinson, A. S., Deegan, F. M., et al. (2019). Hydrothermal alteration of andesitic lava domes can lead to explosive volcanic behaviour. *Nature Communications*, *10*(1), 1–10. <https://doi.org/10.1038/s41467-019-13102-8>
- Heap, M. J., & Violay, M. E. (2021). The mechanical behaviour and failure modes of volcanic rocks: A review. *Bulletin of Volcanology*, *83*(5), 1–47. <https://doi.org/10.1007/s00445-021-01447-2>
- Hicks, T. W., Pine, R. J., Willis-Richards, J., Xu, S., Jupe, A. J., & Rodrigues, N. E. V. (1996). A hydro-thermo-mechanical numerical model for HDR geothermal reservoir evaluation. *International Journal of Rock Mechanics and Mining Sciences*, *33*(5), 499–511. [https://doi.org/10.1016/0148-9062\(96\)00002-2](https://doi.org/10.1016/0148-9062(96)00002-2)
- Hjartardóttir, Á. R., Einarsson, P., Bramham, E., & Wright, T. J. (2012). The Krafla fissure swarm, Iceland, and its formation by rifting events. *Bulletin of Volcanology*, *74*(9), 2139–2153. <https://doi.org/10.1007/s00445-012-0659-0>
- Huenges, E. & Ledru, P. (Eds.) (2011). *Geothermal energy systems: Exploration, development, and utilization*. John Wiley & Sons.
- Hurwitz, S., Kipp, K. L., Ingebritsen, S. E., & Reid, M. E. (2003). Groundwater flow, heat transport, and water table position within volcanic edifices: Implications for volcanic processes in the Cascade Range. *Journal of Geophysical Research*, *108*(B12), 2557. <https://doi.org/10.1029/2003jb002565>
- Ikari, M. J., Saffer, D. M., & Marone, C. (2009). Frictional and hydrologic properties of clay-rich fault gouge. *Journal of Geophysical Research*, *114*(B5), B05409. <https://doi.org/10.1029/2008jb006089>
- Ingebritsen, S. E., Geiger, S., Hurwitz, S., & Driesner, T. (2010). Numerical simulation of magmatic hydrothermal systems. *Reviews of Geophysics*, *48*(1), RG1002. <https://doi.org/10.1029/2009rg000287>
- Inoue, A. (1995). Formation of clay minerals in hydrothermal environments. In *Origin and mineralogy of clays: Clays and the environment* (pp. 268–329).
- Klug, C., & Cashman, K. V. (1996). Permeability development in vesiculating magmas: Implications for fragmentation. *Bulletin of Volcanology*, *58*(2), 87–100. <https://doi.org/10.1007/s004450050128>
- Koyaguchi, T., Scheu, B., Mitani, N. K., & Melnik, O. (2008). A fragmentation criterion for highly viscous bubbly magmas estimated from shock tube experiments. *Journal of Volcanology and Geothermal Research*, *178*(1), 58–71. <https://doi.org/10.1016/j.jvolgeores.2008.02.008>
- Kristmannsdóttir, H. (1979). Alteration of basaltic rocks by hydrothermal-activity at 100–300 C. In *Developments in sedimentology* (Vol. 27, pp. 359–367). Elsevier. [https://doi.org/10.1016/s0070-4571\(08\)70732-5](https://doi.org/10.1016/s0070-4571(08)70732-5)
- Kushnir, A. R., Heap, M. J., & Baud, P. (2018). Assessing the role of fractures on the permeability of the Permo-Triassic sandstones at the Soultz-sous-Forêts (France) geothermal site. *Geothermics*, *74*, 181–189. <https://doi.org/10.1016/j.geothermics.2018.03.009>
- Kushnir, A. R., Martel, C., Bourdier, J. L., Heap, M. J., Reuschlé, T., Erdmann, S., et al. (2016). Probing permeability and microstructure: Unravelling the role of a low-permeability dome on the explosivity of Merapi (Indonesia). *Journal of Volcanology and Geothermal Research*, *316*, 56–71. <https://doi.org/10.1016/j.jvolgeores.2016.02.012>
- Lévy, L., Gibert, B., Sigmundsson, F., Flóvenz, Ó. G., Hersir, G. P., Briole, P., & Pezard, P. A. (2018). The role of smectites in the electrical conductivity of active hydrothermal systems: Electrical properties of core samples from Krafla volcano, Iceland. *Geophysical Journal International*, *215*(3), 1558–1582. <https://doi.org/10.1093/gji/ggy342>
- Loaiza, S., Fortin, J., Schubnel, A., Guéguen, Y., Vinciguerra, S., & Moreira, M. (2012). Mechanical behavior and localized failure modes in a porous basalt from the Azores. *Geophysical Research Letters*, *39*(19), L19304. <https://doi.org/10.1029/2012gl053218>
- Lockner, D. A., & Morrow, C. A. (2008). Energy dissipation in Calico Hills tuff due to pore collapse. *AGU Fall Meeting Abstracts*, 2008, T51A–T1856.
- Manning, C. E., & Ingebritsen, S. E. (1999). Permeability of the continental crust: Implications of geothermal data and metamorphic systems. *Reviews of Geophysics*, *37*(1), 127–150. <https://doi.org/10.1029/1998rg900002>
- Marmoni, G. M., Martino, S., Heap, M. J., & Reuschlé, T. (2017). Gravitational slope-deformation of a resurgent caldera: New insights from the mechanical behaviour of Mt. Nuovo tuffs (Ischia Island, Italy). *Journal of Volcanology and Geothermal Research*, *345*, 1–20. <https://doi.org/10.1016/j.jvolgeores.2017.07.019>
- Martel, C., Dingwell, D. B., Spieler, O., Pichavant, M., & Wilke, M. (2001). Experimental fragmentation of crystal-and vesicle-bearing silicic melts. *Bulletin of Volcanology*, *63*(6), 398–405. <https://doi.org/10.1007/s004450100157>
- Meng, F., Baud, P., Ge, H., & Wong, T.-F. (2019). The effect of stress on limestone permeability and effective stress behavior of damaged samples. *Journal of Geophysical Research: Solid Earth*, *124*(1), 376–399. <https://doi.org/10.1029/2018jb016526>
- Min, K. B., Jing, L., & Stephansson, O. (2004). Determining the equivalent permeability tensor for fractured rock masses using a stochastic REV approach: Method and application to the field data from Sellafeld, UK. *Hydrogeology Journal*, *12*(5), 497–510. <https://doi.org/10.1007/s10040-004-0331-7>
- Mitchell, T. M., & Faulkner, D. R. (2012). Towards quantifying the matrix permeability of fault damage zones in low porosity rocks. *Earth and Planetary Science Letters*, *339*, 24–31. <https://doi.org/10.1016/j.epsl.2012.05.014>

- Mordensky, S. P., Villeneuve, M. C., Kennedy, B. M., Heap, M. J., Gravley, D. M., Farquharson, J. I., & Reuschlé, T. (2018). Physical and mechanical property relationships of a shallow intrusion and volcanic host rock, Pinnacle Ridge, Mt. Ruapehu, New Zealand. *Journal of Volcanology and Geothermal Research*, 359, 1–20. <https://doi.org/10.1016/j.jvolgeores.2018.05.020>
- Mortensen, A. K., Egilson, P., Gautason, B., Árnadóttir, S., & Guðmundsson, Á. (2014). Stratigraphy, alteration mineralogy, permeability and temperature conditions of well IDDP-1, Krafla, NE-Iceland. *Geothermics*, 49, 31–41. <https://doi.org/10.1016/j.geothermics.2013.09.013>
- Mueller, S., Melnik, O., Spieler, O., Scheu, B., & Dingwell, D. B. (2005). Permeability and degassing of dome lavas undergoing rapid decompression: An experimental determination. *Bulletin of Volcanology*, 67(6), 526–538. <https://doi.org/10.1007/s00445-004-0392-4>
- Nara, Y., Meredith, P. G., Yoneda, T., & Kaneko, K. (2011). Influence of macro-fractures and micro-fractures on permeability and elastic wave velocities in basalt at elevated pressure. *Tectonophysics*, 503(1–2), 52–59. <https://doi.org/10.1016/j.tecto.2010.09.027>
- Nara, Y., Morimoto, K., Hiroyoshi, N., Yoneda, T., Kaneko, K., & Benson, P. M. (2012). Influence of relative humidity on fracture toughness of rock: Implications for subcritical crack growth. *International Journal of Solids and Structures*, 49(18), 2471–2481. <https://doi.org/10.1016/j.ijsolstr.2012.05.009>
- Nelson, P. H. (1994). Permeability-porosity relationships in sedimentary rocks. *Log Analyst*, 35(03).
- Noël, C., Baud, P., & Violay, M. (2021b). Effect of water on sandstone's fracture toughness and frictional parameters: Brittle strength constraints. *International Journal of Rock Mechanics and Mining Sciences*, 147, 104916. <https://doi.org/10.1016/j.ijrmm.2021.104916>
- Noël, C., Passelègue, F. X., & Violay, M. (2021a). Brittle faulting of ductile rock induced by pore fluid pressure build-up. *Journal of Geophysical Research: Solid Earth*, 126(3), e2020JB021331. <https://doi.org/10.1029/2020jb021331>
- Ophelm, J. A., & Guðmundsson, A. (1989). Formation and geometry of fractures, and related volcanism, of the Krafla fissure swarm, northeast Iceland. *Geological Society of America Bulletin*, 101(12), 1608–1622. [https://doi.org/10.1130/0016-7606\(1989\)101<1608:fagofa>2.3.co;2](https://doi.org/10.1130/0016-7606(1989)101<1608:fagofa>2.3.co;2)
- Palladino, D., Gaeta, M., & Marra, F. (2001). A large K-foiditic hydromagmatic eruption from the early activity of the Alban Hills Volcanic District, Italy. *Bulletin of Volcanology*, 63(5), 345–359. <https://doi.org/10.1007/s004450100150>
- Pope, E. C., Bird, D. K., Amorrison, S., & Giroud, N. (2016). Hydrogeology of the Krafla geothermal system, northeast Iceland. *Geofluids*, 16(1), 175–197. <https://doi.org/10.1111/gfl.12142>
- Reid, M. E. (2004). Massive collapse of volcano edifices triggered by hydrothermal pressurization. *Geology*, 32(5), 373–376. <https://doi.org/10.1130/g20300.1>
- Reinsch, T., Dobson, P., Asanuma, H., Huenges, E., Poletto, F., & Sanjuan, B. (2017). Utilizing supercritical geothermal systems: A review of past ventures and ongoing research activities. *Geothermal Energy*, 5(1), 1–25. <https://doi.org/10.1186/s40517-017-0075-y>
- Rust, A. C., & Cashman, K. V. (2004). Permeability of vesicular silicic magma: Inertial and hysteresis effects. *Earth and Planetary Science Letters*, 228(1–2), 93–107. <https://doi.org/10.1016/j.epsl.2004.09.025>
- Saar, M. O., & Manga, M. (1999). Permeability-porosity relationship in vesicular basalts. *Geophysical Research Letters*, 26(1), 111–114. <https://doi.org/10.1029/1998gl900256>
- Saemundsson, K., & Geology of the Krafla system (1991). In A. Gardarsson & P. Einarsson (Eds.), *The natural history of lake Myvatn, The Icelandic natural history society, Reykjavik, Iceland* (pp. 24–95). (In Icelandic).
- Sammel, E. A., Ingebritsen, S. E., & Mariner, R. H. (1988). The hydrothermal system at Newberry volcano, Oregon. *Journal of Geophysical Research*, 93(B9), 10149–10162. <https://doi.org/10.1029/jb093ib09p10149>
- Sammis, C. G., & Ashby, M. F. (1986). The failure of brittle porous solids under compressive stress states. *Acta Metallurgica*, 34(3), 511–526. [https://doi.org/10.1016/0001-6160\(86\)90087-8](https://doi.org/10.1016/0001-6160(86)90087-8)
- Sæmundsson, K., Hjartarson, Á., Kaldal, I., Sigurgeirsson, M. A., Kristinsson, S. G., & Vikingsson, S. (2012). Geological map of the Northern Volcanic Zone, Iceland, Northern Part. Iceland Geosurvey and Landsvirkjun, scale 1:100,000.
- Segall, P., & Fitzgerald, S. D. (1998). A note on induced stress changes in hydrocarbon and geothermal reservoirs. *Tectonophysics*, 289(1–3), 117–128. [https://doi.org/10.1016/s0040-1951\(97\)00311-9](https://doi.org/10.1016/s0040-1951(97)00311-9)
- Shimada, M. (2000). *Mechanical behaviour of rocks under high pressure conditions* (Vol. 2). CRC Press.
- Siratovich, P. A., Heap, M. J., Villeneuve, M. C., Cole, J. W., & Reuschlé, T. (2014). Physical property relationships of the Rotokawa Andesite, a significant geothermal reservoir rock in the Taupo Volcanic Zone, New Zealand. *Geothermal Energy*, 2(1), 1–31.
- Spieler, O., Kennedy, B., Kueppers, U., Dingwell, D. B., Scheu, B., & Taddeucci, J. (2004). The fragmentation threshold of pyroclastic rocks. *Earth and Planetary Science Letters*, 226(1–2), 139–148. <https://doi.org/10.1016/j.epsl.2004.07.016>
- Sruoga, P., Rubinstein, N., & Hinterwimmer, G. (2004). Porosity and permeability in volcanic rocks: A case study on the Serie Tobáfera, South Patagonia, Argentina. *Journal of Volcanology and Geothermal Research*, 132(1), 31–43. [https://doi.org/10.1016/s0377-0273\(03\)00419-0](https://doi.org/10.1016/s0377-0273(03)00419-0)
- Stanchits, S., Vinciguerra, S., & Dresen, G. (2006). Ultrasonic velocities, acoustic emission characteristics and crack damage of basalt and granite. *Pure and Applied Geophysics*, 163(5), 975–994. <https://doi.org/10.1007/s00024-006-0059-5>
- Terakawa, T. (2014). Evolution of pore fluid pressures in a stimulated geothermal reservoir inferred from earthquake focal mechanisms. *Geophysical Research Letters*, 41(21), 7468–7476. <https://doi.org/10.1002/2014gl061908>
- Todesco, M., Chiodini, G., & Macedonio, G. (2003). Monitoring and modelling hydrothermal fluid emission at La Solfatara (Phlegrean Fields, Italy). An interdisciplinary approach to the study of diffuse degassing. *Journal of Volcanology and Geothermal Research*, 125(1–2), 57–79. [https://doi.org/10.1016/s0377-0273\(03\)00089-1](https://doi.org/10.1016/s0377-0273(03)00089-1)
- Todesco, M., Rutqvist, J., Chiodini, G., Pruess, K., & Oldenburg, C. M. (2004). Modeling of recent volcanic episodes at Phlegrean Fields (Italy): Geochemical variations and ground deformation. *Geothermics*, 33(4), 531–547. <https://doi.org/10.1016/j.geothermics.2003.08.014>
- Utada, M. (2001). Zeolites in hydrothermally altered rocks. *Reviews in Mineralogy and Geochemistry*, 45(1), 305–322. <https://doi.org/10.2138/rmg.2001.45.10>
- Vairé, E., Heap, M. J., Baud, P., & van Wyk de Vries, B. (2024). Quantifying the physical and mechanical heterogeneity of porous volcanic rocks from the Chaîne des Puys (Massif Central, France). *Bulletin of Volcanology*, 86(5), 49. <https://doi.org/10.1007/s00445-024-01742-8>
- Vajdova, V., Baud, P., & Wong, T. F. (2004). Permeability evolution during localized deformation in Bentheim sandstone. *Journal of Geophysical Research*, 109(B10), B10406. <https://doi.org/10.1029/2003jb002942>
- Vallier, B., Magnenet, V., Schmittbuhl, J., & Fond, C. (2019). Large scale hydro-thermal circulation in the deep geothermal reservoir of Soultz-sous-Forêts (France). *Geothermics*, 78, 154–169. <https://doi.org/10.1016/j.geothermics.2018.12.002>
- Vanorio, T., Prasad, M., Patella, D., & Nur, A. (2002). Ultrasonic velocity measurements in volcanic rocks: Correlation with microtexture. *Geophysical Journal International*, 149(1), 22–36. <https://doi.org/10.1046/j.0956-540x.2001.01580.x>
- Vasseur, J., & Wadsworth, F. B. (2017). Sphere models for pore geometry and fluid permeability in heterogeneous magmas. *Bulletin of Volcanology*, 79(11), 1–15. <https://doi.org/10.1007/s00445-017-1165-1>
- Vinciguerra, S., Del Gaudio, P., Mariucci, M. T., Marra, F., Meredith, P. G., Montone, P., et al. (2009). Physical properties of tuffs from a scientific borehole at Alban hills volcanic district (central Italy). *Tectonophysics*, 471(1–2), 161–169. <https://doi.org/10.1016/j.tecto.2008.08.010>

- Vinciguerra, S., Trovato, C., Meredith, P. G., & Benson, P. M. (2005). Relating seismic velocities, thermal cracking and permeability in Mt. Etna and Iceland basalts. *International Journal of Rock Mechanics and Mining Sciences*, *42*(7–8), 900–910. <https://doi.org/10.1016/j.ijrmms.2005.05.022>
- Violay, M., Heap, M. J., Acosta, M., & Madonna, C. (2017). Porosity evolution at the brittle-ductile transition in the continental crust: Implications for deep hydro-geothermal circulation. *Scientific Reports*, *7*(1), 1–10. <https://doi.org/10.1038/s41598-017-08108-5>
- Wadsworth, F. B., Vasseur, J., Scheu, B., Kendrick, J. E., Lavallée, Y., & Dingwell, D. B. (2016). Universal scaling of fluid permeability during volcanic welding and sediment diagenesis. *Geology*, *44*(3), 219–222. <https://doi.org/10.1130/g37559.1>
- Wang, J., Jung, W., Li, Y., & Ghassemi, A. (2016). Geomechanical characterization of Newberry Tuff. *Geothermics*, *63*, 74–96. <https://doi.org/10.1016/j.geothermics.2016.01.016>
- Weaver, J., Eggertsson, G. H., Utley, J. E., Wallace, P. A., Lamur, A., Kendrick, J. E., et al. (2020). Thermal lability of hyaloclastite in the Krafla geothermal reservoir, Iceland: The impact of phyllosilicates on permeability and rock strength. *Geofluids*, *2020*, 1–20. <https://doi.org/10.1155/2020/9057193>
- Wong, T.-F., & Baud, P. (2012). The brittle-ductile transition in porous rock: A review. *Journal of Structural Geology*, *44*, 25–53. <https://doi.org/10.1016/j.jsg.2012.07.010>
- Wong, T.-F., David, C., & Zhu, W. (1997). The transition from brittle faulting to cataclastic flow in porous sandstones: Mechanical deformation. *Journal of Geophysical Research*, *102*(B2), 3009–3025. <https://doi.org/10.1029/96jb03281>
- Wright, H. M., Cashman, K. V., Gottesfeld, E. H., & Roberts, J. J. (2009). Pore structure of volcanic clasts: Measurements of permeability and electrical conductivity. *Earth and Planetary Science Letters*, *280*(1–4), 93–104. <https://doi.org/10.1016/j.epsl.2009.01.023>
- Wyering, L. D., Villeneuve, M. C., Wallis, I. C., Siratovich, P. A., Kennedy, B. M., Gravley, D. M., & Cant, J. L. (2014). Mechanical and physical properties of hydrothermally altered rocks, Taupo Volcanic Zone, New Zealand. *Journal of Volcanology and Geothermal Research*, *288*, 76–93. <https://doi.org/10.1016/j.jvolgeores.2014.10.008>
- Yale, D. P. (1984). Network modelling of flow, storage and deformation in porous rocks, Ph.D. Thesis. Stanford University.
- Zhang, Y. (1999). A criterion for the fragmentation of bubbly magma based on brittle failure theory. *Nature*, *402*(6762), 648–650. <https://doi.org/10.1038/45210>
- Zhu, W., Baud, P., Vinciguerra, S., & Wong, T.-F. (2011). Micromechanics of brittle faulting and cataclastic flow in Alban Hills tuff. *Journal of Geophysical Research*, *116*(B6), B06209. <https://doi.org/10.1029/2010jb008046>
- Zhu, W., Baud, P., Vinciguerra, S., & Wong, T.-F. (2016). Micromechanics of brittle faulting and cataclastic flow in Mount Etna basalt. *Journal of Geophysical Research: Solid Earth*, *121*(6), 4268–4289. <https://doi.org/10.1002/2016jb012826>
- Zhu, W., Baud, P., & Wong, T.-F. (2010). Micromechanics of cataclastic pore collapse in limestone. *Journal of Geophysical Research*, *115*(B4), B04405. <https://doi.org/10.1029/2009jb006610>
- Zhu, W., & Wong, T.-F. (1997). The transition from brittle faulting to cataclastic flow: Permeability evolution. *Journal of Geophysical Research*, *102*(B2), 3027–3041. <https://doi.org/10.1029/96jb03282>
- Zoback, M. D., & Byerlee, J. D. (1975). The effect of microcrack dilatancy on the permeability of Westerly granite. *Journal of Geophysical Research*, *80*(5), 752–755. <https://doi.org/10.1029/jb080i005p00752>